rijksuniversiteit groningen / faculty of mathematics and natural sciences

Bachelor research project
Astronomy, Mathematics, Physics
1 July 2012

Analysis of Betti Numbers and Persistence Diagrams of 2-Dimensional Gaussian Random Fields

Kapteyn Astronomical Institute,
Johan Bernoulli Institute
& Centre for Theoretical Physics,

University of Groningen

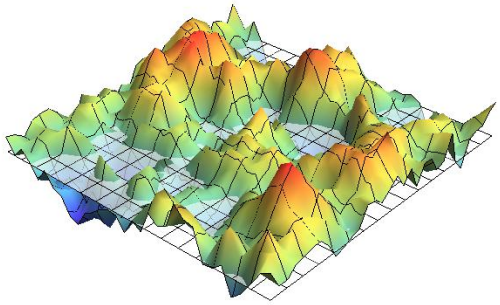

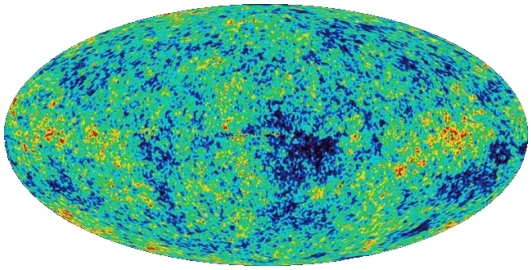

Authors:
Job Feldbrugge and Matti van Engelen

Supervisors:
Prof. dr. M.A.M. van de Weijgaert, Kapteyn Astronomical Institute
Prof. dr. G. Vegter, Johan Bernoulli Institute
Prof. dr E. Pallante, Centre for Theoretical Physics

Analysis of Betti Numbers and Persistence Diagrams of 2-Dimensional Gaussian Random Fields

Job Feldbrugge and Matti van Engelen

Kapteyn Astronomical Institute, Johan Bernoulli Institute & Centre for Theoretical Physics

University of Groningen

1 July 2012

Abstract

In order to unravel the high-energy physics of the early universe, several methods have been proposed to study the Cosmic Microwave Background (CMB). Current methods have posed bounds on the strength of non-Gaussianities in the CMB, but have so far not succeeded in constraining inflationary physics [8, 37, 23, 2, 38, 6, 21, 24]. This is one of the major open problems in cosmology and particle physics. In this thesis we present a novel method of analyzing the CMB, using homological measures. We use Betti numbers and persistence diagrams to analyze Gaussian random fields, by considering both analytical and numerical approaches. We will attempt to extend this method to non-Gaussian random fields, in order to differentiate between inflationary models.

Using existing statistical tools [19, 31] to obtain information about Gaussian random fields, we propose an analytical fitting formula for the Betti numbers of Gaussian random fields. Furthermore, we introduce a new formalism to analytically predict persistence diagrams. Finally we show that persistence diagrams are a promising approach to analyze non-Gaussianities, using realizations of Gaussian random fields.

Concluding, persistence diagrams are potentially a major tool in analyzing the CMB, by putting constraints on the amount of non-Gaussianities and thus on the inflationary physics of the universe.

Contents

Acknowledgements

The authors would like to thank prof. dr. M.A.M. van de Weijgaert for his guidance and support for new ideas during the project. We would like to thank prof. dr E. Pallante and prof. dr. G. Vegter for their guidance and helpful mathematical discussions.

Furthermore we would like to thank drs. M. Wintraecken for his close collaboration, helpful discussions and insight in the calculations of the statistics of Gaussian random fields. We also thank drs. P. Pranav, for his help on the numerical calculations and for the discussion on the interpretations of Betti numbers and persistence diagrams during our project.

Finally we would like to thank the Kapteyn institute for letting us use their computer group, and especially Eite Tiesinga for his help on implementing the numerical calculations on the computer cluster using Condor.

Chapter 1

Introduction

In this thesis we propose a novel method to analyze the Cosmic Microwave Background (CMB) as a probe of inflationary physics. According to the current standard model of cosmology (ΛCDM), 300.000 years after the big bang, the universe had cooled to a temperature of about 3000 K, enough to become transparent. The light emitted by the universe at this time can today be observed as the CMB, a uniform and isotropic blackbody source. Deviations of this isotropic blackbody source have been observed and can be modeled very well by a Gaussian random field, which is completely characterized by its power spectrum. The observed power spectrum of the CMB seems to be in agreement with the power spectrum predicted by the ΛCDM model and thus the classical ΛCDM model gives a good approximation of post-CMB physics.

However, the high-energy physics present during inflation at the early stages of the universe remain unknown, because many different inflationary models can reproduce the power spectrum of the CMB. Nevertheless, different inflationary models predict deviations in the Gaussian random field, called non-Gaussianities. These non-Gaussianities are characterized by a function called the bispectrum. The amount of non-Gaussianities is denoted by f_{NL}, where a larger value of f_{NL} denotes a higher amount of non-Gaussianities. In this thesis we restrict ourselves to so-called local non-Gaussianities. Knowledge about the non-Gaussianities in the CMB can pose constraints on the physics in the inflationary epoch.

Although many attempts have been made to calculate the amount of non-Gaussianities in the CMB, see for example [8, 37, 23, 2, 38, 6, 21, 24], the current bounds on f_{NL} are still too large to draw any solid conclusions about inflationary physics. Although the data from the Planck satellite will make the construction of better bounds possible, it might still take a long time before inflationary physics will be well-understood.

Our approach to analyze Gaussian random fields and non-Gaussianities is based on homology theory, focusing on Betti numbers and Persistence diagrams. The Betti numbers and persistence diagrams are a characterization of the homology of a Gaussian random field. By making a filtration of the Gaussian random field, using superlevel sets, we analyze the Betti numbers and persistence diagrams as a signature of the field. In order to statistically predict these signatures we approximate the Morse-Smale complex

of the filtrated Gaussian random field by a simplicial complex, of which we consequently calculate the homology. This leads to a fitting formula to predict the Betti numbers of a Gaussian random field. Additionally we introduce a novel method of predicting persistence diagrams of Gaussian random fields. Finally, we use numerical methods to analyze persistence diagrams of Gaussian random fields with different power spectra and Gaussian random fields with deviations in the form of local non-Gaussianities. The obtained results imply that persistence diagrams are a potentially sensitive probe to non-Gaussianities.

This thesis consists of three parts. In the first part we give an introduction to cosmology, inflationary physics and non-Gaussianities (chapter 2 and 3). We then introduce Gaussian random fields (chapter 4 and 5), simplicial complexes and the algebraic topology used to analyze simplicial complexes (chapter 6 and 7). In the second part we statistically predict Betti numbers of Gaussian random fields, using critical point expected values. This leads to a formula predicting Betti numbers of Gaussian random fields, given its power spectrum (chapter 8). Moreover, a new formalism is introduced to predict the persistence diagrams of a Gaussian random field. Although we have succeeded in constructing such a formalism, further research has to be pursued in order to complete this formalism (chapter 9). In the third part of our thesis we numerically analyze the persistence diagrams of Gaussian random fields, on which local non-Gaussianities are imposed (chapter 10). This leads to the conclusion that homology theory could form a sensitive probe to non-Gaussianities in Gaussian random fields. Finally, we summarize our results and list our future research topics in chapter 11.

Part I

Background

Chapter 2

Physics in Cosmology

Cosmology is one of the oldest branches of science. For centuries, mankind has been trying to understand the origin, nature and eventually the end of our universe. For a long time, cosmology remained in the realm of religion and philosophy. However, in 1916, Albert Einstein changed this for good by publishing his theory of general relativity. General relativity became the framework in which precise cosmological predictions could be made, making cosmology a physical discipline.

According to Einstein, space and time are dynamical quantities. This also made the universe itself dynamic. The universe could be expanding or contracting, originating, and even ending at some definite time. However, the scientific community was not yet ready for a dynamical universe when general relativity appeared. Einstein introduced a cosmological constant to stabilize his universe and remove the dynamics. A few years later observations of receding galaxies by Hubble confirmed the dynamical behavior predicted by general relativity. After Hubble's observations Einstein removed his cosmological constant and declared it to be his greatest blunder. This became the starting point of a physical debate about the evolution of the universe. Is the universe a stable object which has always existed, or did it have a beginning and would it someday even end?

The debate about the evolution of the universe was finally decided in 1964 by accidental observations of the two radio astronomers Arno Penzias and Robert Wilson. Around 1964, Penzias and Wilson had started the construction of a radio telescope to perform satellite communication experiments. During there observations they observed an excess noise of about 3 Kelvin, which they could not remove or account for. After a telephone call with professor Robert Dicke at Princeton University, the noise was found to be a remnant of an early hot phase of the universe, for which Robert Dicke was looking. This remnant is nowadays called the Cosmic Microwave Background radiation (CMB). The CMB is the basis of one of the main arguments for why our universe has an origin, nowadays called the Big Bang. This discovery led to a Nobel prize in physics for Penzias and Wilson in 1974.

The CMB seemed to contain a vast amount of information about our Universe. Many more detailed observations of the CMB followed. The most recent publicly available mea-

surements were made by the Wilkinson Microwave Anisotropy Probe satellite (WMAP) between October 2001 and October 2010. In May 2009 the European Space Agency (ESA) launched the Planck satellite which probes the CMB in even more detail. The Planck data has however not yet been released.

Extensive measurements of the CMB have unleashed a revolution in cosmology. It is the earliest observable image of our universe and has had a great influence on the development of the Big Bang theory and structure formation models. There are however reasons to expect that the CMB encrypts even more physical knowledge. Between the Big Bang and the time of last ionization, which produced the CMB, many different physical models can account for current observations. In order to differentiate between these models, one can search for deviations on the predicted CMB, called non-Gaussianities in the CMB. In this thesis we introduce a novel approach to detect non-Gaussianities, using homology. This chapter will therefore be devoted to an introduction to early physical models, including inflation, emphasizing the creation of the CMB and the possibility of non-Gaussianities in the CMB. The first part of the chapter is intended to be a short summary of well known cosmology. This is done in the style of the book 'Introduction to Cosmology' by Barbara Ryden [36]. The second part is devoted to calculations of the statistics of the CMB as a consequence of inflation theory.

2.1 The Friedmann Equations

In 1905 Einstein published his famous theory of special relativity. According to special relativity the speed of light in vacuum is universal and therefore independent of the velocity of an observer. This is in clear conflict with Newtonian physics, in which one has to add the observer's speed to the speed of light. Special relativity therefore forms a correction to Newton's dynamics when velocities close to the speed of light are considered. Special Relativity has so far been in exact agreement with observations. The introduction of these corrections, however, also led to the inescapable conclusion that space and time, now called spacetime, can be mixed in a very special way and that the speed of light c is the maximum speed at which information can travel.

After the triumph of special relativity a new problem appeared, because Einstein's new theory was in conflict with Newton's law of gravitation. According to Newton, a change in the mass of an object and thus in its gravitational pull, would instantaneously be effective throughout space, whereas special relativity predicted a finite speed limit on information. In order to resolve this issue, Einstein, in 1916, proposed his theory of general relativity to replace Newton's law of gravitation.

According to general relativity energy, momentum and pressure densities described in the energy momentum tensor $T_{\mu\nu}$ possess the power to bend spacetime described by the metric $g_{\mu\nu}$, the Ricci tensor $R_{\mu\nu}$ and the Ricci curvature scalar R. The bended spacetime in turn influences the movement of objects and therefore influences the energy distribution. The exact interplay between energy and spacetime is described by the

Einstein field equations:

$$R_{\mu\nu} - \frac{1}{2}Rg_{\mu\nu} = \frac{8\pi G}{c^4}T_{\mu\nu}, \text{ with } \mu, \nu = 0, 1, 2, 3,$$

where G is Newton's gravitational constant and c is the speed of light in vacuum.

The Einstein field equations form a complicated system of nonlinear differential equations, which contain solutions describing physical situations with fast-moving or strongly gravitating objects such as black holes. However it can also model the evolution of the universe as a whole. Assuming a completely homogeneous and isotropic universe, nowadays part of the cosmological principle, Alexander Friedmann, in 1922, and later independently Georges Lemaître, in 1927, solved the Einstein field equations. The Einstein field equations for a homogeneous and isotropic universe are called the Friedmann equations and describe the evolution of the universe as a function of its energy content

$$\begin{aligned} H^2 = \left(\frac{\dot{a}}{a}\right)^2 &= \frac{8\pi G}{3}\rho - \frac{kc^2}{R_0^2 a^2}, \\ 0 &= \dot{\rho} + 3\frac{\dot{a}}{a}(\rho + Pc^2), \\ \frac{\ddot{a}}{a} &= -\frac{4\pi G}{3}\left(\rho + \frac{3P}{c^2}\right). \end{aligned}$$

In this equation a denotes the scale of the universe, $\dot{a} = \frac{da}{dt}$ and $\ddot{a} = \frac{d^2a}{dt^2}$ its time derivatives, H is the Hubble parameter known from the Hubble law, ρ denotes the sum of the energy densities (composed out of matter, radiation and dark energy), while $k = 0, 1$ or -1 for a flat, a spherical or a hyperbolic universe respectively. The factor R_0 denotes the current radius of curvature. The factor P in the second equation describes the pressure in the universe. In order to completely solve the Friedmann equations, one has to know the nature of the energy densities making up the energy content curving the universe. The behavior of energy during the evolution of our universe is encoded in the second Friedmann equation in combination with the equation of state $P = \omega\rho$. For baryonic and cold dark matter ω is well approximated by 0, while for radiation $\omega = 1/3$ and for dark energy $-1 \leq \omega \leq -\frac{1}{3}$ is not precisely known but approximately -1. The presence of the dark energy source is assumed in order to explain the present accelerating expansion of our universe. The equations of state in combination with the second Friedmann equation lead to matter diluting like a^{-3}, and radiation diluting like a^{-4} in an expanding universe. The dark energy content with equation of state $\omega = -1$ remains constant.

Assuming the equation of state for dark energy $\omega = -1$, the Friedmann equations can be rewritten as:

$$\frac{H^2}{H_0^2} = \frac{\Omega_{r,0}}{a^4} + \frac{\Omega_{m,0}}{a^3} + \Omega_{\Lambda,0} + \frac{1 - \Omega_0}{a^2},$$

with Hubble parameter H, current Hubble parameter H_0, current radiation density $\Omega_{r,0} = \rho_{r,0}/\rho_{c,0}$, current matter density $\Omega_{m,0} = \rho_{m,0}/\rho_{c,0}$, current dark energy density

$\Omega_{\Lambda,0} = \rho_{\Lambda,0}/\rho_{c,0}$ and current energy density $\Omega_0 = \Omega_{r,0} + \Omega_{m,0} + \Omega_{\Lambda,0}$. The current critical density $\rho_{c,0} = \frac{3H_0^2}{8\pi G}$ is the energy density necessary to make our universe flat ($k = 0$).

This description of our universe is different from the Newtonian view because according to the Friedmann equations the scale factor and therefore the effective size of the universe can change in time. A universe can originate in a Big Bang at a scale ($a = 0$), expand ($\dot{a} > 0$), contract ($\dot{a} < 0$), and end at a definite time ($a = 0$). Originally Einstein did not appreciate this dynamical view of the universe. He introduced an extra term in his equations which made a nearly constant and therefore made his model static. However, after Edwin Hubble discovered systematically receding galaxies in 1927, implying a non vanishing H and $\dot{a}$, Einstein removed his stabilizing term. He thus introduced a completely new way to understand our universe.

2.2 The Cosmic Microwave Background

The debate about the evolution of the universe was for a large part resolved in 1964 with the discovery of the Cosmic Microwave Background radiation (CMB). If the universe is dynamic and has an origin, science would like to measure the remnants of this event. The CMB is now understood to be a remnant of the early universe, forming evidence for the big bang. A detailed analysis of the CMB has provided a vast amount of insight and will potentially tell us a lot more about the early universe in the near future. The most recent observation of the Cosmic Microwave Background, publicly released in 2010, has been made by the Wilkinson Microwave Anisotropy Probe satellite (WMAP). While analyzing the data, one first recovers a completely isotropic perfect blackbody spectrum of $2.725K$ on the sky (see figure 2.1 for observations by the Cosmic Background Explorer (COBE)). Such an isotropic perfect blackbody spectrum implies an extremely hot phase in the early stage of our universe.

Analyzing the data further by evaluating the temperature corresponding to the blackbody spectrum for every pixel on the sky and subtracting the mean temperature, a dipole appears in the measurements around $4mK$ (see figure 2.2 obtained from the COBE observations). This dipole can directly be explained as a Doppler shift of the light, caused by the motion of the Milky way in the Local group, the motion of the sun in the Milky way and the motion of the earth around the sun. The line in the center of the image is caused by the many stars in the plane of the Milky way.

After correcting for the Doppler shifts, one can look even closer into the data for deviations of about $10^{-5}K$ (see figure 2.3). These tiny fluctuations in the temperature field can be interpreted as density fluctuations in a primordial phase of our universe. In practice, the deviations in the Cosmic Microwave Background radiation with respect to the mean temperature and dipole are a subject of ongoing research in cosmology. In this thesis these tiny deviations are often denoted by the name Cosmic Microwave Background radiation (CMB).

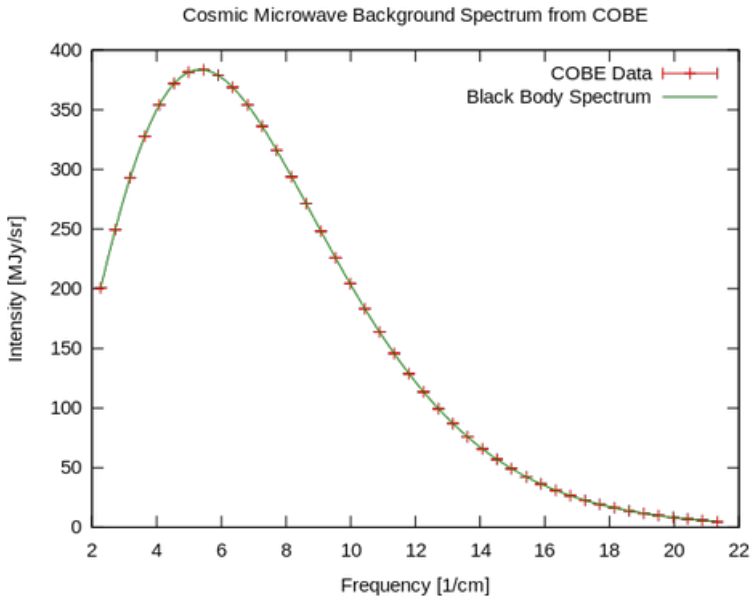

Figure 2.1: The spectrum of the Cosmic Microwave Background radiation, observed by the Cosmic Background Explorer (COBE). (from NASA)

2.2.1 Lambda-Cold Dark Matter Model

The analysis of the deviations in the CMB has led to the conclusion that the CMB is largely homogeneous and isotropic. This makes the solutions of the Friedmannn equations a valid approximation of the evolution of our universe. A more detailed investigation of the deviations shows that the information in the CMB is mainly encrypted in its two point correlation function or equivalently the power spectrum (see figure 2.4 for WMAP observations). The power spectrum is the Fourier transform of the two-point correlation function and describes the amplitude of a certain angular scale in the observations (see chapter 4 for a detailed explanation). The shape of the power spectrum of the CMB can be accurately predicted by cosmological models. The current standard model of cosmology states that we live in a nearly flat universe ($k = 0$), containing a dark energy density ($\Omega_\Lambda = 0.73$) and a cold dark matter and baryionic matter density ($\Omega_m = 0.27$). This model, often abbreviated by ΛCDM, predicts a power spectrum denoted by the red line in figure 2.4. According to current CMB observations this model is in good agreement with observations.

In this thesis we approximate this power spectrum by the fitting formula proposed by Bardeen et al. [19], abbreviated as the BBKS power spectrum. This power spectrum is used for 3-dimensional density distributions, in contrast with the power spectrum shown in figure 2.4, which is based on spherical harmonics. The power spectrum is given by

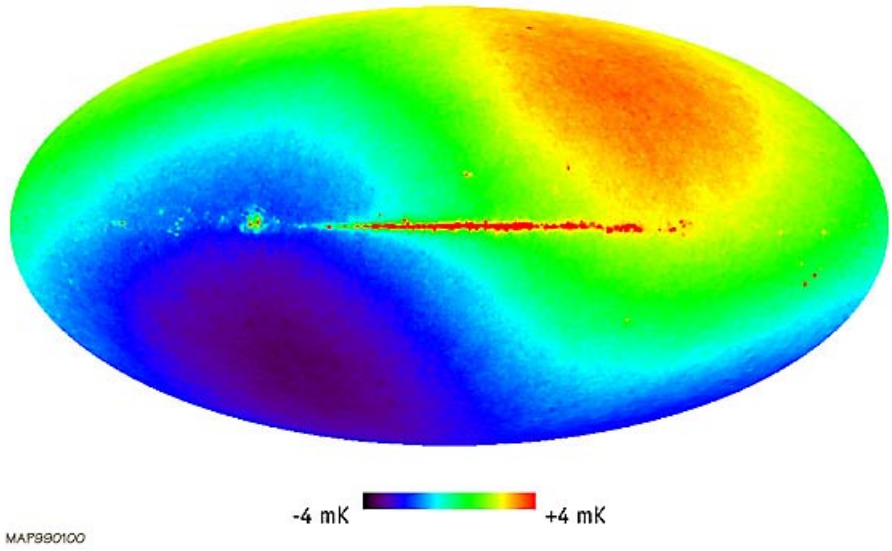

Figure 2.2: Deviations of the Cosmic Microwave Background with respect to the mean temperature observed by the Cosmic Background Explorer (COBE). (from NASA)

the formula:

$$P(k) = k^n T^2(k),\ T(k) = \frac{\log(1+2.34q)}{2.34q}[1+3.89q+(16.1q)^2+(5.4q)^3+(6.71q)^4]^{-1/4},$$

where $q = k/(\Omega_0 h^2\ Mpc^{-1})$, h is the current Hubble parameter divided by 100, Ω_0 is the current total energy density and n is a fine tuning parameter. Although more accurate approximations of the initial power spectrum exist we use the BBKS power spectrum as a first approximation.

2.3 Inflation Theory

The standard model of cosmology (ΛCDM) is in good agreement with current observations. However, it fails to explain two problems, called the flatness and the horizon problem. These problems can be solved using inflation theory as explained in this section.

2.3.1 Problems in the ΛCDM Model

The first problem in the ΛCDM model we consider is the flatness problem. According to the ΛCDM model we live in a spatially flat universe, $\Omega_0 \approx 1$. Observational evidence of CMB anisotropy is consistent with the value

$$|1-\Omega_0| \leq 0.2.$$

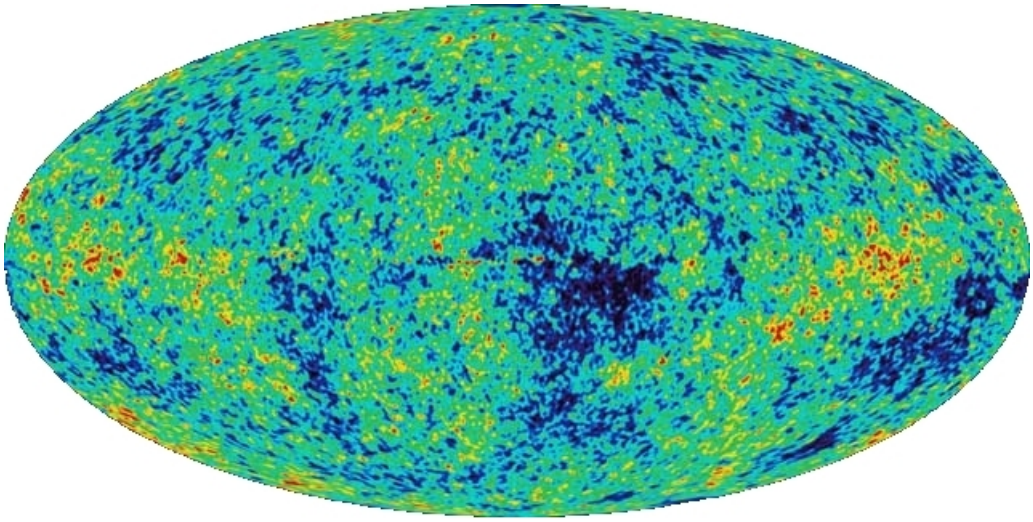

Figure 2.3: Temperature deviations in the CMB with respect to the mean temperature, corrected for the dipole. These observations have been made by WMAP. (from NASA)

However, according to the Friedmann equations this implies that at the time of $\Omega_m = \Omega_r$, the density of the universe had to be

$$|1 - \Omega| \leq 2 \times 10^{-4},$$

and at the time of the formation of the CMB

$$|1 - \Omega| \leq 3 \times 10^{-14}.$$

At even earlier times, Ω would have to be even closer to 1 to make our current universe flat. This problem is not in conflict with the ΛCDM model. However it would require an incredibly precise choice of parameters at the time of the Big Bang. It would be far more satisfactory if there exists a physical mechanism to flatten the early universe.

The flatness problem is accompanied by the horizon problem which concerns the extreme isotropy and homogeneity of the CMB at large scales. In order to illustrate this problem we consider two antipodal points on the CMB. The proper distance from earth to the CMB (surface of last scattering) is

$$d_p(t_0) = c \int_{t_{\text{CMB}}}^{t_0} \frac{dt}{a(t)}.$$

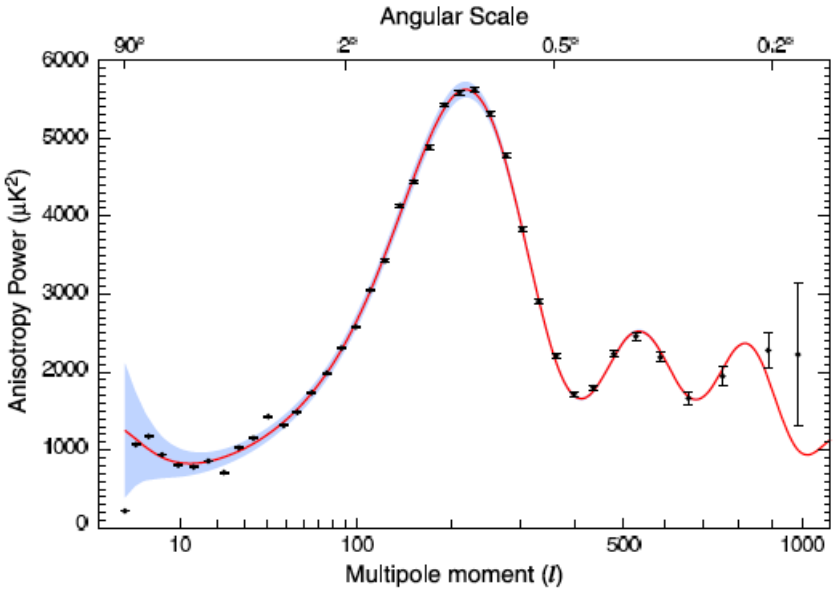

Figure 2.4: The power spectrum of the CMB. These observations have been made by WMAP [25].

Because the CMB was created a long time ago ($t_0 \gg t_{CMB}$), the current proper distance from earth to the CMB is only slightly smaller than the current horizon distance $d_{hor}(t_0)$. According to the ΛCDM model $d_p(t_0) = 0.98 d_{hor}(t_0)$. Two antipodal points on the CMB are currently separated by a proper distance of $1.96 d_{hor}(t_0)$. Since this distance is greater than the current horizon distance, the two points on the CMB have to be causally disconnected. They have had no possibility to exchange information, let al.one get in thermal equilibrium. Nevertheless, the temperature of the CMB is extremely homogeneous across the sky. The extreme isotropy of the CMB is even more remarkable. According to the ΛCDM model the horizon distance at the time of last scattering can be approximated by

$$d_{hor}(t_{\text{CMB}}) = \frac{2c}{H(t_{\text{CMB}})} \approx 0.4\ Mpc.$$

The distance to the surface of last scattering is approximately $d_A = 13\ Mpc$. Therefore the angular size of the horizon at the time of last scattering of the currently observed CMB is given by

$$\theta_{hor} = \frac{d_{hor}(t_{\text{CMB}})}{d_A} \approx \frac{0.4\ Mpc}{13\ Mpc} \approx 0.03 \text{ rad} \approx 2^\circ$$

Therefore points on the CMB separated by an angle θ greater then 2° were causally disconnected during the formation of the CMB. However the CMB shows that at scales $\theta > 2^\circ$ anisotropies in the surface of last scattering $\delta T/T$ are in the order of 10^{-5}. Hence

a physical mechanism to explain this extreme isotropy would give a more complete understanding of cosmology.

2.3.2 Inflation Theory

The two problems can be solved using inflation theory. Inflation theory can be seen as the hypothesis that there has been a period in the early history of our universe where our universe underwent a great expansion. A rapid expansion would flatten the pre-inflationary universe in such a way that a flat universe at the current time is possible, solving the flatness problem. It would make it possible for points in the CMB to be in thermal equilibrium before inflation and, nevertheless to be causally disconnected in our current universe, solving the horizon problem.

Inflation is an extremely convenient way of solving the problems which arise in the epoch before the creation of the CMB in the ΛCDM model. However the mechanism which causes the expansion is difficult to physically describe. During inflation the universe went through an exponential expansion. According to the Friedmannn equations this is only possible if $\rho + 3p < 0$. Both the equations of state for matter and radiation do not satisfy this condition. However the condition can be achieved by a spatially homogeneous scalar field ϕ in a potential V. The energy density of such a field is given by:

$$\rho_\phi = \frac{1}{2}\left(\frac{d\phi}{dt}\right)^2 + V(\phi).$$

The pressure of a scalar field ϕ is given by:

$$p_\phi = \frac{1}{2}\left(\frac{d\phi}{dt}\right)^2 - V(\phi).$$

From these equations it follows that the scalar field ϕ can cause an exponential expansion if:

$$\left(\frac{d\phi}{dt}\right)^2 < V(\phi).$$

Physically this condition implies a field in which the kinetic energy is always smaller than its potential energy. This condition is therefore called slow-roll [43] (see figure 2.5). On first sight this seems to be an extremely elegant theory with a simple way of deducing the correct physics: find a scalar field in high energy physics with a corresponding potential which satisfies this condition. The physics at this energy scale is however largely unknown and there are many potentials $V(\phi)$ satisfying the slow-roll condition. Furthermore, inflation can also be caused by multiple fields with an even more complicated potential. Up to now, many inflationary theories have been able to reproduce the power spectrum of the CMB, leaving inflationary physics an open problem. However, some inflationary models also predict higher order correlation functions in the CMB,

called non-Gaussianities, possibly providing a method to differentiate between different models. In the next section, inflation theory is developed using a quantum approach, developed by B.I. Rigopoulos et al. [33, 35, 34]. This approach is used to predict power spectra and non-Gaussianities for inflationary models.

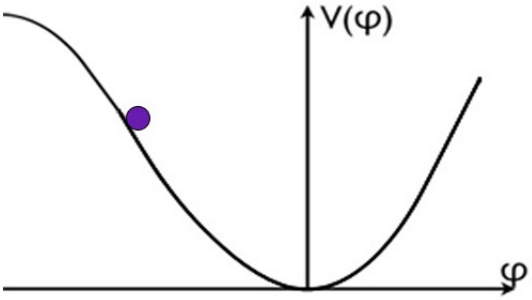

Figure 2.5: The potential of a scalar inflaton field has a typical shape depicted in above figure.

In the next section we will consider a few different inflationary theories and search for measurable features of these theories to distinguishing them.

2.4 Non-Gaussianities

In the discussion above, only classical cosmology is considered. This forms a good approximation of the evolution of our universe after the creation of the CMB. The content of the universe was relatively cool and the observable universe was already relatively large. In this section we consider the physics of inflation before the creation of the CMB. During the epoch of inflation the universe was extremely small and hot. We therefore apply quantum physics to the above described Friedmannn equations. Using this approach we predict the initial fluctuations occurring in the CMB.

During inflation the universe experienced a very rapid expansion. According to conventional cosmology this makes the comoving observable universe (and therefore the comoving Hubble radius $(aH)^{-1}$) shrink. All astrophysical structures which are formed within an observable universe are therefore soon stretched to superhorizon scales. These superhorizon features persist during this epoch because different parts of the features cannot communicate with each other. At a later stage, the comoving Hubble radius increases again, letting these superhorizon features re-enter the observable universe. The important structures in the CMB can therefore be assumed to be on a superhorizon scale during inflation. We will therefore use a long-wavelength approximation to analyze predictions of the CMB [33, 35, 34].

As described above, inflation theories are in general based on N scalar fields ϕ^A, with $A = 1, 2, \ldots, N$, in combination with a potential V. If the long-wavelength approximation is valid, we can drop all second order spatial derivatives. In this approximation, we

will describe spacetime by the general metric

$$\mathrm{d}s^2 = -N^2(t,\mathbf{x})\mathrm{d}t^2 + a^2(t,\mathbf{x})h_{ij}(\mathbf{x})\mathrm{d}x^i\mathrm{d}x^j,$$

in which N is the lapse function, a is the local scale factor and h_{ij} is a local spatial metric with unit determinant. For superhorizon features it can be shown that h_{ij} becomes constant. The local scale factor a determines the scale to which the universe has expanded. The lapse function N can be seen as a reparametrization of time. If we now couple the scalar fields ϕ^A to the Einstein field equations via the energy momentum tensor,

$$T_{\mu\nu} = G_{AB}\partial_\mu\phi^A\partial_\nu\phi^B - g_{\mu\nu}\left(\frac{1}{2}G_{AB}\partial^\lambda\phi^A\partial_\lambda\phi^B + V\right)$$

and re-derive the Friedmannn equations while applying the long-wavelength approximation by dropping all second order spatial derivatives, we obtain a set of coupled nonlinear differential equations which model inflation. This model describes the evolution of the early universe as a function of the general field metric G_{AB}, the scalar field ϕ^A, for $A = 1, 2, \ldots, N$ and the potential V in the long-wavelength limit [35].

Using these differential equations one can statistically predict the properties of the CMB [34]. For single field inflationary models ($N = 1$) this results in a standard power spectrum of the fluctuations ζ in the predicted CMB:

$$\langle|\zeta(k)|^2\rangle = \frac{\kappa^2}{4}\frac{1}{k^3}\frac{H_{\mathcal{H}}}{\epsilon_{\mathcal{H}}},$$

with

$$\kappa^2 = 8\pi G,\ \epsilon = \frac{\kappa^2\Pi^2}{2H^2} \text{ and } \Pi = \dot{\phi}/N.$$

The variables $\epsilon_{\mathcal{H}}$ and $H_{\mathcal{H}}$ denote the parameters ϵ and H evaluated at horizon crossing. This 2-point correlation function or power spectrum completely characterizes the field if the CMB is a Gaussian random field (mathematically defined in chapter 4). Deviations from such a Gaussian random field are characterized to lowest order by the 3-point correlation function or bispectrum.

Equivalently to the power spectrum, the 3-point correlation function and therefore the bispectrum is given by

$$\langle\zeta(\mathbf{k}_1)\zeta(\mathbf{k}_2)\zeta(\mathbf{k}_3)\rangle = (2\pi)^3\delta^3(\mathbf{k}_1+\mathbf{k}_2+\mathbf{k}_3)[f(\mathbf{k}_1,\mathbf{k}_2) + f(\mathbf{k}_1,\mathbf{k}_3) + f(\mathbf{k}_2,\mathbf{k}_3)],$$

with

$$f(\mathbf{k}_1,\mathbf{k}_2) = \frac{\kappa^4}{16}\frac{1}{|\mathbf{k}_1|^3|\mathbf{k}_2|^3}\frac{H_{\mathcal{H}_1}^2}{\epsilon_{\mathcal{H}_1}}\frac{H_{\mathcal{H}_2}^2}{\epsilon_{\mathcal{H}_2}}\left[\left((2\epsilon_{\mathcal{H}_2}+\eta_{\mathcal{H}_2})\frac{|\mathbf{k}_1|^2}{|\mathbf{k}_1|^2+|\mathbf{k}_2|^2}\frac{|\mathbf{k}_1|^2+\mathbf{k}_1\cdot\mathbf{k}_2}{|\mathbf{k}_1+\mathbf{k}_2|^2}\right) + (\mathbf{k}_1 \leftrightarrow \mathbf{k}_2)\right].$$

In this equation,

$$\eta = -3 - \frac{\partial V/\partial \phi}{H\Pi},$$

with $\mathcal{H}_1$ and $\mathcal{H}_2$ corresponding to evaluations at horizon crossing with $\mathbf{k}_1$ and $\mathbf{k}_2$, respectively.

This formalism makes it possible to predict two and three point correlation functions as a function of the potential V or equivalently the slow-roll parameters ϵ and η. In practice these slow-roll parameters have to be small to make sure that the potential field V is flat enough to ensure the necessary inflationary epoch. The analysis summarized above however does not require small roll parameters. The analysis is solely based on the assumption that important features are on a superhorizon scale during inflation, implying the long-wavelength approximation.

2.4.1 Bispectra Shapes

In general, any function $B : \mathbb{R}^+ \times \mathbb{R}^+ \times \mathbb{R}^+ \to \mathbb{R}$, with $\mathbb{R}^+ = \{r \in \mathbb{R} | r \geq 0\}$, and $B(|\mathbf{k}_1|, |\mathbf{k}_2|, |\mathbf{k}_3|)$ with $\mathbf{k}_1 + \mathbf{k}_2 + \mathbf{k}_3 = 0$ can be seen as a bispectrum. Because tightly constraining observations of non-Gaussianities have not yet been made, in practice the scientific community considers four different bispectra: local, enfolded, equilateral and orthogonal. More complicated situations can be constructed by combining these four bispectra.

The simplest form of non-Gaussianities is local non-Gaussianities. Local non-Gaussianities are most intuitively described by their construction:

$$\Phi^{NG} = \Phi^G + f_{NL}\bigg((\Phi^G)^2 - \langle \Phi^G \rangle^2\bigg),$$

in which Φ^G is a Gaussian random field, f_{NL} is the strength of the local non-Gaussianities and Φ^{NG} is the constructed non-Gaussian field. This kind of non-Gaussianity can be characterized by the bispectrum:

$$B(k_1, k_2, k_3) = 2f_{NL}[P(k_1)P(k_2) + P(k_2)P(k_3) + P(k_1)P(k_3)],$$

with P the power spectrum of the Gaussian random field of interest. The equilateral, enfolded and orthogonal non-Gaussianities have no analog simple construction formula. The equilateral non-Gaussianities are therefore defined by the bispectrum:

$$\begin{aligned} B(k_1, k_2, k_3) =& 6f_{NL}(-(P(k_1)P(k_2) + P(k_2)P(k_3) + P(k_1)P(k_3)) - 2(P(k_1)P(k_2)P(k_3))^{2/3} \\ &+ (P(k_1)^{2/3}P(k_2)^{2/3}P(k_3) + P(k_1)^{2/3}P(k_2)P(k_3)^{2/3} + \dots)). \end{aligned}$$

The enfolded and orthogonal non-Gaussianities are equivalently defined by respectively:

$$\begin{aligned} B(k_1, k_2, k_3) =& 6f_{NL}((P(k_1)P(k_2) + P(k_2)P(k_3) + P(k_1)P(k_3)) + 3(P(k_1)P(k_2)P(k_3))^{2/3} \\ &- (P(k_1)^{2/3}P(k_2)^{2/3}P(k_3) + P(k_1)^{2/3}P(k_2)P(k_3)^{2/3} + \dots)), \end{aligned}$$

and

$$B(k_1,k_2,k_3) = 6f_{NL}(-3(P(k_1)P(k_2)+P(k_2)P(k_3)+P(k_1)P(k_3)) - 8(P(k_1)P(k_2)P(k_3))^{2/3} + 3(P(k_1)^{2/3}P(k_2)^{2/3}P(k_3)+P(k_1)^{2/3}P(k_2)P(k_3)^{2/3}+\dots)).$$

The dots in the bispectra denote cyclic permutations [42].

By analyzing the linear combination of bispectra and strength f_{NL} of non-Gaussianity in the CMB, one can completely characterize the non-Gaussian character of the CMB up to the 3-point correlation function. For more precise measurements (in the future) we will have to extend this analysis to higher order correlation functions.

Chapter 3

Current Constraints on non-Gaussianities and Physical Models

Since the discovery of the Cosmic Microwave Background (CMB) by the two radio astronomers Arno Penzias and Robert Wilson in 1964, the CMB has been probed by many more detailed surveys. In 1978, Penzias and Wilson were awarded the Nobel prize for their discovery. In November 1989, NASA launched the Coscmic Background Explorer (COBE), satellite dedicated to the investigation of the CMB. The principal investigators of the COBE, George Smoot and John Mather, concluded that the CMB is a nearly perfect blackbody with small anisotropies. Their work resulted in a Nobel prize in 2006. The CMB was further analyzed by the Balloon Observation Of Millimeter Extragalactic Radiation and Geophysics (BOOMERanG) experiment, by lifting a telescope to a height of 42 km making a high quality map of the CMB. In 1999, these observations led to the conclusion that we live in an extremely flat universe. The work of COBE was succeeded in 2001 by the Wilkinson Microwave Anisotropy Probe (WMAP). This satellite has made a more detailed full sky map of the anisotropy of the CMB. The WMAP data is now seen as the most accurate measurement of the CMB. In 2009, ESA launched the Planck satellite which will probably lead to an improvement on the WMAP survey by reaching a three times higher resolution and a ten times higher sensitivity. The final data observed by the Planck satellite are expected to be publicly available by the end of 2012.

WMAP observations of the CMB have revealed the anisotropy statistics up to the 2-point correlation function. See figure 2.4 for the equivalent power spectrum. The higher order correlation functions are not yet completely known. In this chapter we consider the bounds on the 3-point correlation function, or equivalently the bispectrum, and the possible implications that constraints on the bispectrum can have on the physical models of the evolution of the universe.

3.1 Bispectra Measurements

During the last ten years scientists have made many attempts to measure the bispectrum in the CMB. Minkowski functionals, methods as 'Bispectra Optimal', the spherical Mexican hat wavelet and the skewness of the power spectrum have been used on COBE, BOOMERanG and WMAP datasets. However, up to now, none of the approaches have led to any decisive conclusion about whether the CMB contains any non-Gaussianities and if it does, to which type they belong and which strength they have [43, 7]. One can only conclude that if present, non-Gaussianities have to be small. For example, one of the most constraining measurements of non-Gaussianities in the 7 year WMAP data results in $f_{NL} = 2.5 \pm 3.0$ for the local bispectrum, $f_{NL} = 37 \pm 18$ for the equilateral and $f_{NL} = 25 \pm 14$ for the orthogonal bispectrum [22, 7]. This constrains the CMB, but it is not enough to draw definite conclusions. The data of the Planck satellite are supposed to constrain f_{NL} up to a resolution of about 5, possibly giving a more definite answer to the question whether the CMB contains non-Gaussianities [26].

3.2 Implications for Inflation Theory

The observed power spectrum of the CMB can be predicted by many inflationary models, both single field and multi field models. The existence or absence of deviations in the form of non-Gaussianities can be seen as the primary tool to differentiate between different inflationary models.

Simple inflationary models generate negligible amount of non-Gaussianities. In practice, if the following 5 criteria are all satisfied, no non-Gaussianities will be detectable by the WMAP or Planck satellite:

- A single inflation field is responsible for inflation;
- The scalar field has a canonical kinetic energy term in the action;
- The evolution of the scalar field always satisfies the slow-roll condition;
- The universe was in a so called Bunch-Davies vacuum before inflation started;
- The evolution of the universe during inflation is well described be general relativity.

This list is based on calculations done by Maldacena [28]. In this section we shortly sketch the proof of this statement, which he made in [5].

The action of a single field inflation model with a canonical kinetic energy term can be written as:

$$S = \int \mathrm{d}^4x\sqrt{-g}\left[\frac{M_P}{2}R - \frac{1}{2}g^{\mu\nu}\partial_\mu\phi\partial_\nu\phi - V(\phi)\right].$$

In this equation the field ϕ and the potential V are coupled to Einstein gravity via the determinant of the metric tensor g, with the metric signature $(-1, 1, 1, 1)$. Here

$M_P = (8\pi G)^{-1/2}$ is the reduced Planck mass. Assuming that the slow-roll conditions are satisfied ($\epsilon, \eta \ll 1$, with the slow-roll parameters defined in chapter 2), the action simplified. If one now uses this simplified action to compute the bispectrum of the CMB and assumes the Bunch-Davies vacuum as the initial state, it can be shown that the amount of non-Gaussianities is approximately $f_{NL} = \mathcal{O}(\eta)$. In practice the slow-roll parameter η is in the order of 0.01. The amount of non-Gaussianities produced by a single field inflation model with a canonical kinetic energy term is therefore $f_{NL} = \mathcal{O}(0.01)$. Even if one takes into account non-linear effects in the late evolution of the CMB, the amount of non-Gaussianities will not exceed $f_{NL} = \mathcal{O}(1)$. These non-Gaussianities are well below the sensitivity of the WMAP and below the expected sensitivity of the Planck satellite, which is probably more than 5. Therefore, inflationary models satisfying the above 5 criteria are expected to produce negligible amounts of non-Gaussianities.

However, if non-Gaussianities are observed by the WMAP or Planck experiments, at least one of the 5 simple inflation model assumptions has to be violated. This leads to more complicated inflationary models with multiple possible violations producing measurable amounts of non-Gaussianities:

- multiple scalar fields;
- higher order derivatives in the kinetic term of the action;
- potentials which do not satisfy the slow-roll condition at any time;
- a non Bunch-Davies vacuum before inflation;
- quantum gravity, which acts in a different manner than general relativity in the early universe.

In order to predict the specific non-Gaussianities of an inflationary model, one can use the approach of section 2.4 or other equivalent approaches to calculate the expected non-Gaussian features in the CMB. This can help to explain the observed non-Gaussianities in the CMB and probably help to determine the specific deviations from the single field model with a canonical kinetic energy term [5].

3.2.1 Characteristic Bispectra

Research has been done to translate predicted characteristic features in the CMB to the general behavior of inflation theory. Here we briefly discuss some characteristic features calculated by Chen [5], but the exact calculations are not within the scope of this thesis.

Physically the occurrence of large non-Gaussianities implies large non-linear interactions during inflation. In single field inflation, long wavelength modes which exited the horizon of the observable universe are frozen. Modes within an observable universe oscillate by which non-Gaussianities generally average out. Therefore, large non-linear interactions can only occur when modes have similar wavelengths and exit the horizon around the same time. Theories with higher order derivatives in the kinetic energy

term (violating the second point) have this kind of interactions. Because of the similar wavelengths of these modes, magnitudes, the bispectrum of these theories will be similar to the equilateral bispectrum. Observations of large equilateral non-Gaussianities may therefore suggest a non-canonical term in the action of the scalar field.

The fluctuation amplitudes of massless scalar inflation fields do not decay at superhorizon scales. This is in contrast with massive scalar fields. The superhorizon wavelength modes of massless scalar fields therefore evolve locally. The modes at different positions are separated by a horizon and are independent from each other. This corresponds with local non-Gaussianities. As another possibility, if the state of the universe before inflation is not in the Bunch-Davies vacuum, detailed calculations lead to characteristic enfolded non-Gaussianities [5].

This is however not a one-to-one correspondence between possible inflation theories and bispectra. Distinct inflationary models can produce comparable bispectra, making it even more complex to infer an inflationary theory from an observed power spectrum and bispectrum.

3.3 High Energy Physics

The reason that inflation theory has yet remained a speculative science is because the physics on which it is based is still an area of ongoing research. While the energy scale at which inflation takes place is below the Planck scale ($10^{18}\ GeV$) it exceeds the electroweak energy scale (in the order of TeV) at which the standard model of particle physics operates. Furthermore, there is no evidence that Einstein's theory of general relativity is valid at those scales. A theory which predicts the CMB and its anisotropic fluctuations will therefore be a theory of extremely high energy physics which will possibly combine, in a unified framework, both high energy electroweak interactions with gravity.

The presence or absence of non-Gaussianities in the CMB and, if present, the kind and amount of non-Gaussianities should be seen as a tool to probe the physics during the inflationary epoch of our universe. However, up to now it remains difficult to experimentally determine the non-Gaussianities in the CMB. Possible theories which describe physics at extremely high energy scales are quantum gravity theories such as string theory [20]. There are also other approaches using quantum field theories. One of these approaches for example assume the Higgs potential as a candidate for the inflation potential and calculate inflation and CMB anisotropies using this model [9].

In this thesis a new approach to measure non-Gaussianities in Gaussian random fields is introduced. We demonstrate the sensitivity of this new approach by means of numerical simulations and attempt to find an analytical tool to discriminate between different kinds of non-Gaussianities. This thesis may therefore provide a new method which ultimately could be used to pose constraints on high energy physics models. However, there still remains work to be done until the tool can be applied to the observed CMB and give any concrete results.

Chapter 4

Gaussian Random Fields and non-Gaussianities

After the observation of the Cosmic Microwave Background (CMB) researchers soon discovered tiny fluctuations on the uniform blackbody spectrum of the CMB. These deviations were soon realized to be accurately modeled by a Gaussian random field. In this thesis, we analyze these fluctuations, both by analyzing Gaussian random fields and non-Gaussianities. In this chapter we will provide the necessary mathematical foundation needed to analyze Gaussian random fields and non-Gaussianities.

In 1944, Rice [32] developed the notion of Gaussian random fields, using them to analyze one-dimensional noise in communication devices. In 1957, Longuet-Higgins [27] expanded upon Rice's analysis by looking at 2-dimensional Gaussian random fields in order to model ocean waves. Doroshkevich was one of the first to apply Gaussian random fields to cosmological problems [11]. There are several reasons why a Gaussian random field could be a good description for the CMB, one of them is the central limit theorem. It states that a Gaussian distribution arises whenever there is a variable which is a linear superposition of a large number of independent variables, which are all drawn from the same distribution, which can be assumed in the early universe [1],[19]. Before we can take a look at Gaussian random fields, we will first look at a general random field.

4.1 Random Fields

A random field is a generalization of a stochastic process, where instead of drawing a single statistic (figure 4.1a) from the distribution, multiple statistics are drawn simultaneously (figures 4.1b, 4.1c). These statistics can compose vectors, points on manifolds or any other multidimensional statistic. Here, the statistics which are simultaneously drawn are often correlated in some way (figure 4.1c), and therefore dependent on one another. In this thesis we are interested in drawing functions from a probability distribution, such that any drawn function defines a manifold. Because we are looking at functions describing manifolds, and not at the manifolds themselves, it follows that every linear statistic of the function, drawn from the distribution, has to be distributed by the

(a) A roll of a dice can be seen as a single draw from a probability distribution.

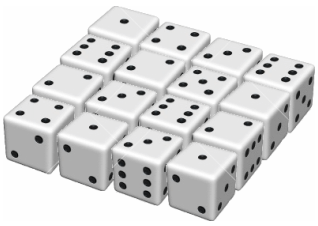

(b) A roll of multiple dice is a simultaneous draw of multiple statistics from a probability distribution. In this figure the dice are not correlated in any way, every dice is rolled independently of every other dice.

(c) A roll of multiple dice which are correlated can be seen as a random field. Compared to figure 4.1b these dice show a clear correlation. The distribution of these dice is clearly smoother than that of the dice in figure 4.1b.

Figure 4.1: An intuitive approach to constructing random fields is shown here.

original distribution. The function drawn from the distribution is called a realization of a random field. For example, both figures 4.1b and 4.1c are realizations of a 4 by 4 statistic, where the values of the field are between 1 and 6.

Concretely this means that a random field f, drawn from a distribution P, has the property that its n-point joint probability function P_n describes the distribution of the linear statistic y_i for $i = 1, 2, \ldots$ of the function f.

4.1.1 Gaussian Random Fields

For a Gaussian random field, which is the only random field we consider in this thesis, the n-point joint probability function is defined as:

$$P_n = \frac{\exp[-\frac{1}{2}\sum_{i,j}\Delta y_i (M^{-1})_{ij}\Delta y_j]}{[(2\pi)^n \det M]^{1/2}}, \tag{4.1}$$

where the covariance matrix M is defined by $M_{ij} = \langle \Delta y_i \Delta y_j^* \rangle$, and $\Delta y_i = y_i - \langle y_i \rangle$, where $\langle ... \rangle$ denotes the average over the field. In this equation * denotes complex conjugation. According to this equation, a Gaussian random field is completely defined by its covariance matrix M. For a 2-dimensional Gaussian random field $f : \mathbb{R}^2 \to \mathbb{R}$ embedded in real flat space, the values of the field in a specific point $\mathbf{r}_i \in \mathbb{R}^2$ $\forall i$, are given by $f(\mathbf{r}_i)$. These values form a natural choice of random variables, with the corresponding n-point joint probability function,

$$P_n = \frac{\exp[-\frac{1}{2}\sum_{i,j} f(\mathbf{r}_i)(M^{-1})_{ij} f(\mathbf{r}_j)]}{[(2\pi)^n \det M]^{1/2}}. \tag{4.2}$$

Intuitively a Gaussian random field can be constructed by rolling an infinite number of dice ($n \to \infty$), where each dice can take on any value in $\mathbb{R}$. Thus every point in

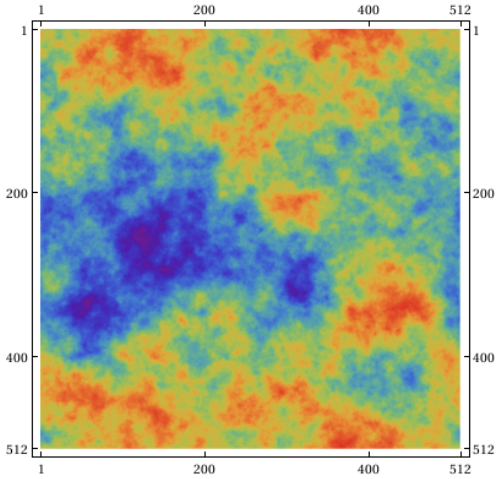

(a) A density plot of a realization of Gaussian random field

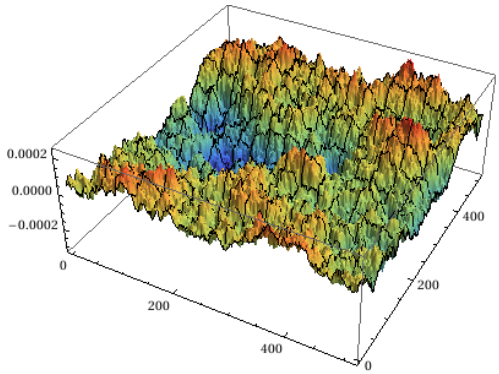

(b) A 3-dimensional plot of a realization of a Gaussian random field

Figure 4.2

$U \subset \mathbb{R}^2$ has a random value, which has a spatial correlation to other nearby field values. This correlation is encoded in the matrix M. An example of a realization of a Gaussian random field can be seen in figure 4.2

4.1.2 Random Gaussian Fields in Euclidean Space

As mentioned in the previous section, Gaussian random fields are completely characterized by the covariance matrix M. Per definition of the covariance matrix, the (i, j)-th element of M is equal to the 2-point correlation function:

Definition 1 (2-point correlation function)**.** *The 2-point correlation function ξ is defined by:*

$$M_{ij} = \xi(x_i, x_j) = \langle f(\boldsymbol{x}_i) f^*(\boldsymbol{x}_j) \rangle.$$

Because of translational and rotational invariances of the Gaussian random field, this correlation function only depends on the distance between the points $\boldsymbol{x}_i$ and $\boldsymbol{x}_j$:

$$M_{ij} = \xi(\boldsymbol{x}_i, \boldsymbol{x}_j) = \xi(|\boldsymbol{x}_i - \boldsymbol{x}_j|)$$

Because M completely defines the Gaussian random field, the 2-point correlation function ξ can also be used to describe the field. As shown by van de Weygaert and Bertschinger [39], the Fourier modes of a Gaussian random field are independent. It is therefore convenient to expand the field in Fourier modes using the power spectrum. We define the Fourier transform to be:

Definition 2 (Fourier Transform)**.** *The 2-dimensional Fourier transform $\hat{f}$ of f is defined as:*

$$f(\boldsymbol{x}) = \int \frac{d\boldsymbol{k}}{(2\pi)^2} \hat{f}(\boldsymbol{k}) e^{-i\boldsymbol{k}\cdot\boldsymbol{x}},$$

for all $\boldsymbol{x}$.

Using this Fourier transform we define the power spectrum $P(k)$:

Definition 3 (Power Spectrum for Fields on a Euclidean Basis)**.** *The power spectrum $P(k)$ on fields with a Euclidean basis is defined as*

$$\langle \hat{f}(\boldsymbol{k}) \hat{f}^*(\boldsymbol{k}') \rangle = (2\pi)^2 P(k) \delta^2(\boldsymbol{k} - \boldsymbol{k}'),$$

where $\delta^2(\boldsymbol{k})$ is the Dirac delta distribution, $k = |\boldsymbol{k}|$, and * denotes complex conjugation.

By expanding the covariance matrix in Fourier space the power spectrum becomes the Fourier transform of the autocorrelation function:

$$\xi(\boldsymbol{x}) = \int \frac{d\boldsymbol{k}}{(2\pi)^2} P(k) e^{-i\boldsymbol{k}\cdot\boldsymbol{x}},$$

for sufficiently smooth power spectra.

4.1.3 Random Gaussian Fields on Spherical Harmonics

Astronomical sky surveys, such as observations of the CMB, are often projected on a 2-dimensional sphere, $\mathbb{S}^2$. So far we have not managed to apply our analysis to the CMB, however we here shortly explain the necessary steps needed to analyze Gaussian random fields on spheres [18]. Calculations on $\mathbb{S}^2$ are often done in a Spherical harmonics basis.

$$f(\hat{\mathbf{n}}) = \sum_{l,m} a_{lm} Y_l^m(\hat{\mathbf{n}}).$$

For such functions one can define a power spectrum analogous to the one in Euclidean space.

Definition 4 (Power Spectrum for Fields on a Spherical Basis)**.** *The power spectrum C_l on fields with a spherical harmonics basis is defined as*

$$\langle a_{l_1 m_1} a_{l_2 m_2} \rangle = C_{l_1} \delta_{l_1 l_2} \delta_{m_1 m_2}, \tag{4.3}$$

with δ_{ij} being the Kronecker delta function.

In practice this leads to the following definition for the power spectrum in spherical harmonics:

$$C_l = \frac{1}{2l+1} \sum_m \langle a_{lm} a_{lm}^* \rangle, \tag{4.4}$$

where * denotes complex conjugation.

4.1.4 Constructing Realizations of Gaussian Random Fields

In order to examine Gaussian random fields numerically, we take multiple draws from a Gaussian random field, called realizations, and examine their properties. Although a GRF is completely defined by its probability density, it is difficult to generate direct realizations. In this section we therefore derive the properties of the Fourier transform of realizations of GRFs and derive a fast algorithm to generate realizations. We apply the method described in [39].

The conventional definition of Gaussian random fields is based on the n-point joint probability density

$$P_n = \frac{\exp[-\frac{1}{2}\sum_{i,j}\Delta y_i (M^{-1})_{ij}\Delta y_j]}{[(2\pi)^n \det M]^{1/2}}. \tag{4.5}$$

If we chose the statistic y_i for $i = 1, \ldots, n$ to be the field values $f(\mathbf{x}_i)$, of a function $f : \mathbb{R}^2 \to \mathbb{R}$ with zero mean, on a grid with equal spatial sampling $\mathbf{x}_i$, the probability density is given by

$$P_n = \frac{\exp[-\frac{1}{2}\sum_{i,j} f(\mathbf{x}_i)(M^{-1})_{ij} f(\mathbf{x}_j)]}{[(2\pi)^n \det M]^{1/2}}.$$

By taking the limit $n \to \infty$ with uniform spatial sampling, the summation can be turned into an integral. The resulting probability density

$$P[f] = Ae^{-S[f]}$$

is similar to the path integral formalism in quantum field theory, with action $S[f]$. In this equation A is a normalization constant, and the action is given by

$$S[f] = \frac{1}{2}\int \mathrm{d}\mathbf{x}_1 \int \mathrm{d}\mathbf{x}_2 f(\mathbf{x}_1) K(\mathbf{x}_1 - \mathbf{x}_2) f(\mathbf{x}_2).$$

The inverse of the covariance matrix M is in this equation substituted by the functional K. This functional is, equivalently to the matrix M, the inverse of the 2-point correlation function $\xi(\mathbf{x})$

$$\int \mathrm{d}\mathbf{x} K(\mathbf{x}_1 - \mathbf{x})\xi(\mathbf{x} - \mathbf{x}_2) = \delta^2(\mathbf{x}_1 - \mathbf{x}_2), \tag{4.6}$$

with the 2-dimensional Dirac delta distribution δ^2, now defined by

$$\delta^2(x) = \int \frac{\mathrm{d}\mathbf{k}}{(2\pi)^2} e^{-i\mathbf{x}\cdot\mathbf{k}}. \tag{4.7}$$

The probability density P can be diagonalized by expressing the action $S[f]$ in terms of the Fourier transform of the field $\hat{f}$. By virtue of the convolution theorem equation 4.6 is equal to

$$\int \frac{\mathrm{d}\mathbf{k}}{(2\pi)^2} \hat{K}(\mathbf{k}) P(k) e^{-i\mathbf{k}\cdot(\mathbf{x}_1 - \mathbf{x}_2)} = \delta^2(\mathbf{x}_1 - \mathbf{x}_2), \tag{4.8}$$

with $\hat{K}$ and P defined by

$$K(\mathbf{x}) = \int \frac{\mathrm{d}\mathbf{k}}{(2\pi)^2} \hat{K}(\mathbf{k}) e^{-i\mathbf{k}\cdot\mathbf{x}}, \text{ and } \xi(\mathbf{x}) = \int \frac{\mathrm{d}\mathbf{k}}{(2\pi)^2} P(|\mathbf{k}|) e^{-i\mathbf{k}\cdot\mathbf{x}}.$$

Substituting the definition of the Dirac delta distribution (equation 4.7) in equation 4.8 implies that $\hat{K}(\mathbf{k}) = 1/P(|\mathbf{k}|)$. Therefore

$$K(\mathbf{x}) = \int \frac{\mathrm{d}\mathbf{k}}{(2\pi)^2} \frac{1}{P(|\mathbf{k}|)} e^{-i\mathbf{k}\cdot\mathbf{x}}.$$

Applying $\hat{K}(\mathbf{k}) = 1/P(|\mathbf{k}|)$ to the double convolution of $S[f]$ gives

$$S[f] = \frac{1}{2} \int \frac{\mathrm{d}\mathbf{k}}{(2\pi)^2} \hat{f}^*(\mathbf{k}) \hat{K}(\mathbf{k}) \hat{f}(\mathbf{k}) = \int \frac{\mathrm{d}\mathbf{k}}{(2\pi)^2} \frac{|\hat{f}(\mathbf{k})|^2}{2P(|\mathbf{k}|)}.$$

Therefore the probability density $P[f]$ for a particular function f can be written in terms of $\hat{f}$ as

$$P[f] = P[\hat{f}] = A \exp\left[- \int \frac{\mathrm{d}\mathbf{k}}{(2\pi)^2} \frac{|\hat{f}(\mathbf{k})|^2}{2P(|\mathbf{k}|)} \right].$$

If we would peruse a similar derivation with a discrete Fourier transform, this would result in

$$P[f] = A \prod \exp\left[- \frac{1}{2} \left(\frac{|\hat{f}(\mathbf{k})|}{\sqrt{L^2 P(|\mathbf{k}|)/2}} \right)^2 \right],$$

with the product over $\mathbf{k}$ iterating over all discrete Fourier modes in a domain of periodicity L, ($\mathbf{k} = \frac{2\pi}{L}(m, n)$, with $(m, n) \in \mathbb{Z}^2$). Note that the function f has a real image and therefore $\hat{f} : \mathbb{R}^2 \to \mathbb{C}$ with $\hat{f}(-\mathbf{k}) = \hat{f}(\mathbf{k})$. From this equation it follows that all Fourier modes are independent (up to symmetry) and normally distributed according to the density

$$P[\hat{f}(\mathbf{k})] = \exp\left[- \frac{1}{2} \left(\frac{|\hat{f}(\mathbf{k})|}{\sqrt{L^2 P(|\mathbf{k}|)/2}} \right)^2 \right].$$

If we therefore draw random complex numbers from this normal distribution, we obtain a Fourier transform of a realization of a GRF. After applying an inverse discrete Fourier transform we finally obtain a realization of a GRF. In practice it is often easier to ignore the symmetry relation $\hat{f}(-\mathbf{k}) = \hat{f}(\mathbf{k})$. Ignoring this constrain, the realization of the GRF becomes a complex function. However, it can be proven that the real and imaginary part of this function are independent Gaussian random fields with a power spectrum given by $P(|\mathbf{k}|)/2$.

4.2 Non-Gaussianities

In Gaussian random fields all information is encoded in the 2-point correlation function ξ or implicitly in its power spectrum P (or C_l). Higher order correlation functions for Gaussian random fields can be decomposed into a combination of 2-point correlation functions using Wick's or Isserlis' theorem [30]:

$$\langle y_1 y_2 \dots y_{2n} \rangle = \sum \prod \langle y_i y_j \rangle, \text{where } \langle y_1 y_2 \dots y_{2n+1} \rangle = 0, \text{ with } n \in \mathbb{N}, \tag{4.9}$$

where $\sum \prod$ is the sum of the product over all distinct ways of partitioning the linear random variables $y_1, \dots, y_n$ into pairs. For example:

$$\langle y_1 y_2 y_3 y_4 \rangle = \langle y_1 y_2 \rangle \langle y_3 y_4 \rangle + \langle y_1 y_3 \rangle \langle y_2 y_4 \rangle + \langle y_1 y_4 \rangle \langle y_2 y_3 \rangle.$$

If deviations on Gaussian random fields occur, this results in new contributions to the higher order correlation functions. If the deviations are small, these deviations are called non-Gaussianities. The field can then be seen as a perturbation on a purely Gaussian random field. These non-Gaussianities can be measured by calculating the 3 and 4-point correlation functions, or equivalently the bispectrum $B(k_1, k_2, k_3)$ or trispectrum $T(k_1, k_2, k_3, k_4)$:

$$\langle \hat{f}(\mathbf{k}_1) \hat{f}(\mathbf{k}_2) \hat{f}(\mathbf{k}_3) \rangle = (2\pi)^2 B(k_1, k_2, k_3) \delta^2(\mathbf{k}_1 + \mathbf{k}_2 + \mathbf{k}_3) \tag{4.10}$$

$$\langle \hat{f}(\mathbf{k}_1) \hat{f}(\mathbf{k}_2) \hat{f}(\mathbf{k}_3) \hat{f}(\mathbf{k}_4) \rangle = (2\pi)^2 T(k_1, k_2, k_3, k_4) \delta^2(\mathbf{k}_1 + \mathbf{k}_2 + \mathbf{k}_3 + \mathbf{k}_4), \tag{4.11}$$

where δ^2 is the 2-dimensional Dirac delta distribution. In this thesis we only consider non-Gaussianities up to bispectra.

4.3 The Ergodic Theorem

For our numerical approach we will be looking at realizations of Gaussian random fields. The ergodic theorem states that a large enough realization of a Gaussian random field, will always represent the power spectrum of the Gaussian random field. This implies that all information of a Gaussian random field can be deduced from a sufficiently large realization of the field. Formally:

Theorem 1 (Ergodic Theorem)**.** *Take any Gaussian random field and pick a realization. Deduce the power spectrum from this realization. Then, with probability* 1*, in the limit as the size of the realization goes to infinity: (a) the power spectrum converges to a limit and (b) that limit is the power spectrum of the Gaussian random field [17].*

Chapter 5

Densities of Critical Points

In this thesis we are interested in the Betti numbers of Gaussian random fields. In our calculations we use the expected density of maxima, saddle points and minima of Gaussian random fields. This means that we use the expected amount of critical points if we were to make a realization of a Gaussian random field given its power spectrum.

Given a Gaussian random field, with its corresponding power spectrum or 2-point correlation function, the expected amount of critical points can be computed using the joint probability function (JPF) that defines the Gaussian random field. Bardeen et al. [19] have computed the expected density of maxima in a Gaussian random field. Here we expand upon their method, following the approach of Gay and Pichon [31], with some minor adjustments. They expand on the approach taken by Bardeen et al. [19], deriving not only the expected density of maxima, but also the statistical counts for saddle points and minima. In this chapter we will not distinguish between Gaussian random fields on a sphere or on a flat space, since the calculation of their critical point densities is similar. Figure 5.1 shows a realization of a 2-dimensional Gaussian random field, clearly showing the importance of maxima and minima in the structure of the Gaussian random field.

5.1 Densities of Critical Points in Random Gaussian Fields

To calculate the density of critical points in a Gaussian random field we will first describe the standard procedure for finding critical points. We then use the JPF to calculate the expected amount of critical points for a given Gaussian random field.

5.1.1 Finding Critical Points in Random Gaussian Fields

A real 2-dimensional Gaussian random field $f : \mathbb{R}^2 \to \mathbb{R}$ has a critical point in $\mathbf{r}_{cri}$ if all of its partial derivatives are zero at $\mathbf{r}_{cri}$. This means that $f_i = \frac{\partial f(\mathbf{r}_{cri})}{\partial r_i} = 0$ for $i = 1, 2$. The nature of the critical point in $\mathbf{r}_{cri}$ is then determined by the eigenvalues of the Hessian

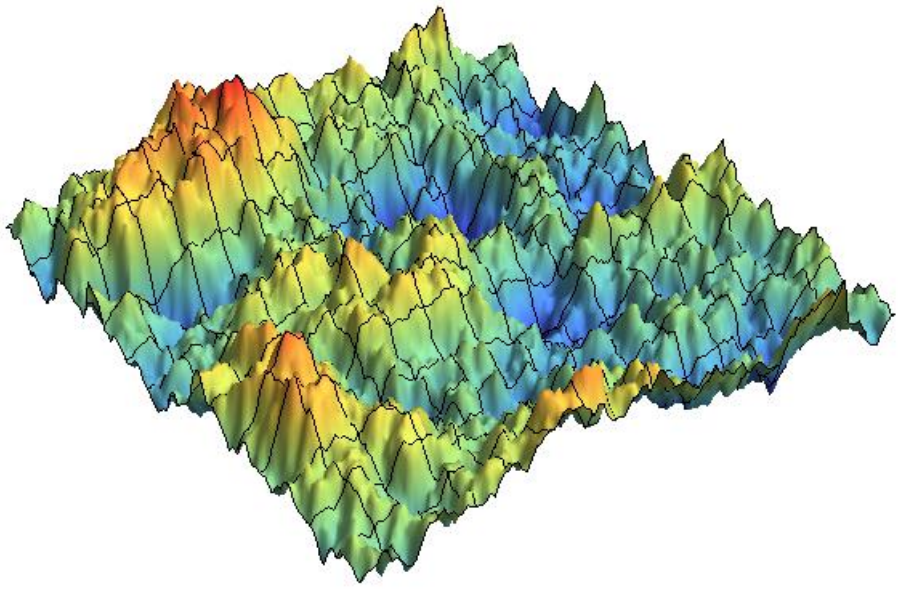

Figure 5.1: A 2-dimensional Gaussian random field, showing the importance of maxima and minima in the overall structure of the field.

matrix in $\mathbf{r}_{cri}$. These eigenvalues are given by:

$$\lambda_{1,2} = \frac{f_{11} + f_{22} \pm \sqrt{(f_{11} - f_{22})^2 + 4f_{12}^2}}{2}, \text{with } f_{ij} = \frac{\partial^2 f(\mathbf{r}_{cri})}{\partial r_i \partial r_j}.$$

Here f is a maximum in $\mathbf{r}_{cri}$ when $\lambda_1 \leq \lambda_2 < 0$, is a saddle point when $\lambda_1 < 0 < \lambda_2$ and it is a minimum when $\lambda_1 \geq \lambda_2 > 0$. From now on we call the number of positive eigenvalues the index of the critical point and denote a critical point with index n as an n-th order critical point. When $\lambda_i = 0$ for $i = 1$ or $i = 2$ (i.e. a singular Hessian) this method is indecisive and one has to consider higher derivatives. This type of critical point is however non-generic and will not influence our computations. Therefore we do not consider them here.

5.1.2 Calculating the Joint Probability Function of a Random Gaussian Field

For the computation of critical point densities we use the eigenvalues of the Hessian computed above, together with the Gaussian random field f and its partial derivatives f_i. The random variables of our field are therefor f, f_i and λ_i, evaluated in $\mathbf{r}_{cri}$. For con-

venience we remove the square root of the eigenvalues by parametrizing the eigenvalues:

$$J_1 = \lambda_1 + \lambda_2 = f_{12} + f_{22} \tag{5.1}$$

$$J_2 = (\lambda_1 - \lambda_2)^2 = (f_{11} - f_{22})^2 + 4f_{12}^2, \tag{5.2}$$

resulting in the random variable $y = (f, f_1, f_2, J_1, J_2)$ in $\mathbf{r}_{cri}$.

By calculating the covariance matrix $M_{ij} = \langle y_i y_j \rangle$ as a function of the power spectrum, we can calculate the joint probability function using the definition of a random Gaussian field. The calculations of the JPF are performed in appendix A for both flat and spherical space. Because, by equation 5.1 and 5.2, the J_i represent the type of critical point we are interested in, we can distinguish between the different types of critical points by choosing appropriate parameter domains. As shown by Gay and Pichon [31], the following parameter domains hold: $f_i = 0, J_1 \in (-\infty, 0), J_2 \in (0, J_1^2)$ corresponds to a maximum; $f_i = 0, J_1 \in (-\infty, \infty), J_2 \in (J_1^2, \infty)$ corresponds to a saddle point and $f_i = 0, J_1 \in (0, \infty), J_2 \in (0, J_1^2)$ corresponds to a minimum. These domains are shown in table 5.1.

critical point of index n	J_1	J_2
0	$(-\infty, 0)$	$(0, J_1^2)$
1	$(-\infty, \infty)$	(J_1^2, ∞)
2	$(0, \infty)$	$(0, J_1^2)$

Table 5.1: Parameter domain of J_1 and J_2 for critical points of index n.

5.1.3 Critical Points Counts of Random Gaussian Fields

In this section we use the JPF obtained in the previous section to find the expected amount of critical points in a Gaussian random field.

In order to estimate the density of critical points of a Gaussian random field $f : \mathbb{R}^2 \to \mathbb{R}$, we define the function:

$$n_{cri}(\mathbf{r}) = \sum_{e \in E} \delta^{(2)}(\mathbf{r} - \mathbf{r}_e) \tag{5.3}$$

for a critical point $\mathbf{r}_e$ in a 2-dimensional Gaussian random field f). Here $\delta^{(2)}$ denotes the 2-dimensional Dirac delta distribution given by

$$\delta^2(\mathbf{x}) = \frac{1}{(2\pi)^2} \int d\mathbf{p}\ e^{i\mathbf{p}\cdot\mathbf{x}}, \text{ with } x \in \mathbb{R}^2$$

and E is the set of critical points of interest. By expanding the field f in a Taylor series around the critical point $\mathbf{r}_e$, we approximate the field in $G = \{\mathbf{r} \in \mathbb{R}^2 \big| \ |\mathbf{r} - \mathbf{r}_e| <$

ϵ, with $\epsilon > 0\}$ by:

$$f(\mathbf{r}) = f(\mathbf{r}_e) + \frac{1}{2}\sum_{i,j}^{2,2} H_{ij}(\mathbf{r}-\mathbf{r}_e)_i(\mathbf{r}-\mathbf{r}_e)_j + \mathcal{O}(|\mathbf{r}-\mathbf{r}_e|^3)$$

$$f_i(\mathbf{r}) = \sum_{j}^{2} H_{ij}(\mathbf{r}-\mathbf{r}_e)_j + \mathcal{O}(|\mathbf{r}-\mathbf{r}_e|^2),$$

Where H is the Hessian of f at $\mathbf{r}_e$, defined by $H_{ij} = f_{ij}(\mathbf{r}_e)$. Assuming that H is non-singular and approximating f up to order $|\mathbf{r}-\mathbf{r}_e|$, valid in G, we can invert the second relation to:

$$\mathbf{r} - \mathbf{r}_e = H^{-1}(\mathbf{r}_e)\nabla f(\mathbf{r}).$$

Applying the Dirac delta function to this difference gives:

$$\delta^{(2)}(\mathbf{r}-\mathbf{r}_e) = |\det\ H(\mathbf{r}_e)|\delta^{(2)}(\nabla f(\mathbf{r})) \text{ for } \mathbf{r} \in G. \tag{5.4}$$

Equation 5.4 will be used to count the amount of critical points in equation 5.3. This implies that the critical point at $\mathbf{r}_e$ should have no contribution to this counting, outside of its ϵ environment. Therefore we set 5.4 equal to 0 in $\mathbb{R}^2\backslash G$. Thus:

$$\delta^{(2)}(\mathbf{r}-\mathbf{r}_e) = |\det\ H(\mathbf{r}_e)|\delta^{(2)}(\nabla f(\mathbf{r})) \text{ for } \mathbf{r} \in \mathbb{R}^2.$$

Substituting this equation in 5.3 gives:

$$n_{cri}(\mathbf{r}) = |\det\ H(r)|\delta^{(2)}(\nabla f(\mathbf{r})).$$

If we average over this function we obtain the expected amount of critical points in the Gaussian random field:

$$\begin{aligned}\langle n_{cri}\rangle &= \iiiint |\det\ H|P(f, f_i = 0, J_i)df\,df_{11}df_{12}df_{22} \\ &= \iiint P(f, f_i = 0, J_i)|J_1^2 - J_2|df\,dJ_1dJ_2.\end{aligned} \tag{5.5}$$

Here $P(f, f_i = 0, J_i)$ is the 1-point JPF, given in appendix A.

Integrating over the right domains of J_1 and J_2 as given by table 5.1 gives the expected value of maxima, saddle points or minima, choosing E appropriately [19, 31].

5.1.4 Critical Points Densities and Total Critical Points

In this thesis we are interested in the density of critical points at a particular field value $f(\mathbf{r}_{cri})$. Figure 5.2 shows a Gaussian random field with a plane intersecting it at 3 different heights. This figure shows that the critical point counts at a certain height ν are good indicators of the overall structure of the Gaussian random field, containing more information than the total amount of critical points in the Gaussian random field.

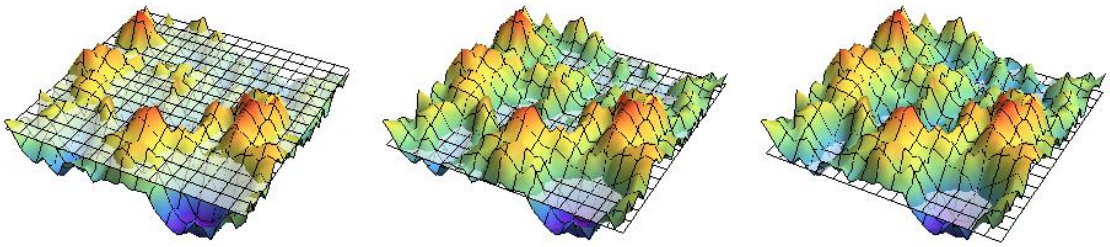

Figure 5.2: A Gaussian random field with a plane intersecting it at three different thresholds ν. The densities of critical points changes substantially when the threshold is lowered. This shows that critical point counts around a certain threshold ν contain information about the structure of the Gaussian random field.

Because we are dealing with 2-dimensional Gaussian random fields, the height of this plane is the field value $f(\mathbf{r})$.

Using equation 5.5 we obtain the following formula for the density of critical points of index i, $\mathcal{N}_i : \mathbb{R} \to \mathbb{R}$, at a level ν:

$$\mathcal{N}_i(\nu) = \iint |\det\ H| P(f, f_j = 0, J_j) |J_1^2 - J_2| dJ_1 dJ_2.$$

Here the index of the critical point of interest is selected by integrating over the appropriate domains for J_1 and J_2 as shown in table 5.1.

Using the above equation we can easily calculate the amount of critical points of index i above a certain threshold ν by integrating:

$$N_i(\nu_0) = \int_{\nu_0}^{\infty} \mathcal{N}_i(\nu) d\nu.$$

The total amount of critical points in a Gaussian random field is therefore:

$$N_i = \int_{-\infty}^{\infty} \mathcal{N}_i(\nu) d\nu.$$

We have now obtained two measures for critical points in Gaussian random fields: $\mathcal{N}_i(\nu)$, which is the density of critical points at a field value ν, and $N_i(\nu_0)$, which is the amount of critical points which have a field value larger than ν_0. Figure 5.3 shows plots of $\mathcal{N}_0(\nu)$, $\mathcal{N}_1(\nu)$ and $\mathcal{N}_2(\nu)$.

5.1.5 Critical Points Count of Constrained Random Gaussian Fields

In this thesis we often look at constrained Gaussian random fields. For example a function which has a maximum with a certain height at a certain position. Given such a field, with a known maximum, we would like to compute the critical point density distribution

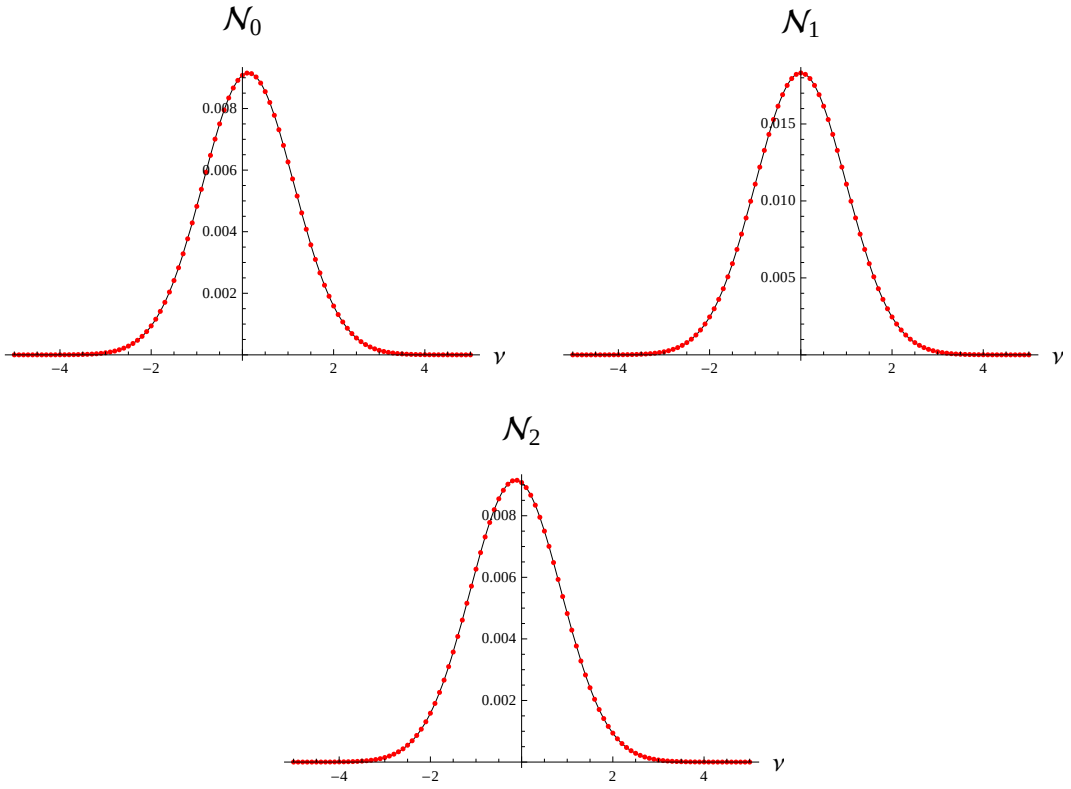

Figure 5.3: Plots of the densities of maxima ($\mathcal{N}_0$), saddle points ($\mathcal{N}_1$) and minima ($\mathcal{N}_2$) at different thresholds ν.

of this constrained Gaussian random field.

The problem we solve in this section is the following conditional probability: given a critical point A at a fixed place $\mathbf{r}_1$ with field value $f(\mathbf{r}_1) = a$ we want to compute the distribution of another critical point B at $\mathbf{r}_2$ with value $f(\mathbf{r}_2) = b$. Due to the translational and rotational invariance of a constrained Gaussian random field, the problem can be reduced to the distribution of a critical point B separated a distance x from a given critical point A. A 1-dimensional illustration can be seen in figure 5.4.

Analogously to the previous section we use the random variable $y = (a, f_i(0), J_i(0), b, f_i(x), J_i(x))$, in which the critical point A corresponds to the arguments $f_i(0)$ and $J_i(0)$ and the critical point B, separated by a distance x from A, corresponds to the arguments $f_i(x)$ and $J_i(x)$. We write the correlation matrix $M_{ij} = \langle y_i y_j \rangle$ in terms of the power spectrum as in appendix A. Using this covariance matrix we calculate the JPF, given

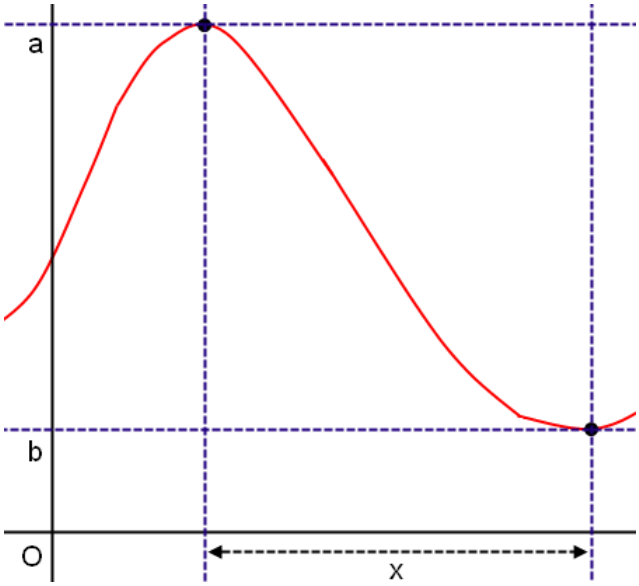

Figure 5.4: An example of a maximum A with $f(\mathbf{r}_1) = a$ and a saddle point B with $f(\mathbf{r}_2) = b$, separated a distance x from each other. By specifying x and A we can obtain the probability distribution function of B by using equation 5.6.

by:

$$p_{ij}(a,b,x) = \iiiint P(a, f_k(0) = 0, J_k(0), b, f_k(x) = 0, J_k(x)) \times (|J_1(0)^2 - J_2(0)| + |J_1(x)^2 - J_2(x)|) dJ_1(0) dJ_2(0) dJ_1(x) dJ_2(x). \tag{5.6}$$

Once more the integral is evaluated by integrating over the appropriate domains of $J_k(0)$ and $J_k(x)$ $(k = 1, 2)$ for the different types of critical points. Here $p_{ij}(a, b, x)$ is the density distribution of a critical point B of index j at $\mathbf{r}_2$ with $f(\mathbf{r}_2) = b$, separated a distance x away from a given critical point A of index i at $\mathbf{r}_1$ with $f(\mathbf{r}_1) = a$.

Concluding, we have obtained expressions for critical point densities for both constrained and unconstrained Gaussian random fields.

Chapter 6

Homology Groups: Betti Numbers and Persistence Diagrams

Algebraic topology is a branch of mathematics which studies topology by means of algebra. We will use this to define and compute homology groups. Homology groups form a mathematical language to express and quantify holes in geometrical objects. In order to compute these homology groups we introduce simplicial complexes on which chain, cycle and boundary groups are defined. Using these groups, Betti numbers and persistence diagrams are introduced, which form a signature of the homology and therefore the topology of a simplicial complex.

These homological measures will be used to calculate the Betti numbers and persistence diagrams of Gaussian random fields. We will numerically and analytically compare the Betti numbers and persistence diagrams of different Gaussian random fields and fields with non-Gaussianities in the coming chapters.

6.1 Algebraic Topology

In this section, the language in which homology groups are expressed is introduced. For a more complete introduction and the proofs of the theorems and group properties see [12].

6.1.1 Simplicial Complexes

This section introduces simplicial complexes, which will later be used to analyze Gaussian random fields. We begin by considering the elements of a d-dimensional simplicial complex:

Definition 5. *(Simplices)*

- *The* 0*-dimensional simplex is a vertex (point) denoted by* v_i*;*
- *The* 1*-dimensional simplex is a line between two vertices,* v_i, v_j*. It is called an edge* e *and is denoted by the vertices which span the edge* $e = v_i v_j$*,* $i \neq j$*;*

- *The 2-dimensional simplex is a face f which is spanned by 3 vertices v_i, v_j, v_k. It is denoted by the 3 vertices which span the face $f = v_i v_j v_k$, with $i \neq j \neq k \neq i$;*
- *The d-dimensional simplex (d-simplex) is spanned by d vertices, $v_{i_1}, v_{i_2}, \ldots, v_{i_d}$. It will generally be called σ and is denoted by $\sigma = v_{i_1} v_{i_2} \ldots v_{i_d}$, with $i_n \neq i_m$ $\forall n, m$ with $n \neq m$.*

A d-dimensional simplicial complex K is the collection of all simplices in a given structure (see figure 6.1 for an example).

6.1.2 Chains

A p-dimensional chain (p-chain) is a collection of simplices. The green elements of figure 6.1 form an example. The chains are formally defined as:

Definition 6. *(Chains)*
Given a simplicial complex K, a p-chain is given by $c = \sum a_i \sigma_i$, in which σ_i are all p-simplices $\in K$, and $a_i \in \mathbb{Z}/2\mathbb{Z}$.

Summation of p-chains $c_1 = a_1\sigma_1$ and $c_2 = a_2\sigma_2$ is defined as $c_1 + c_2 = a_1\sigma_1 + a_2\sigma_2$. When $\sigma_1 = \sigma_2 = \sigma$ this is equivalent to $c_1 + c_2 = (a_1 + a_2)\sigma$, where $a_1 + a_2 \in \mathbb{Z}/2\mathbb{Z}$ and thus $1 + 1 = 0$. The corresponding group of p-chains is defined by:

Definition 7. *(Chain group)*
Given a simplicial complex K, the p-dimensional chain group $C_p = \{c = \sum a_i \sigma_i \ | \sigma_i \in K,\ a_i \in \mathbb{Z}/2\mathbb{Z}$ and $\dim(\sigma_i) = p,\ \forall i\}$.

6.1.3 The Boundary Map

Finally we define the p-dimensional boundary map by:

Definition 8. *(The boundary map)*
Given a p-simplex $\sigma = v_1 \ldots v_p \in K$, the boundary map $\partial_p : C_p \to C_{p-1}$, is defined as $\partial_p \sigma = \sum_{i=0}^{p} [v_1, \ldots, \hat{v}_i, \ldots, v_p]$, in which the vertex with the hat is omitted, $[v_1, \ldots, \hat{v}_i, \ldots, v_p] = v_1 \ldots v_{i-1} v_{i+1} \ldots v_p$.

The boundary map is linear, so for any chain $c = \sum a_i \sigma_i$, the map $\partial_p c = \sum a_i \partial_p \sigma_i$.

In homology theory two specific subsets of C_p play an important role. A p-chain c with a empty boundary, $\partial_p c = 0$, is called a p-cycle (an example is the yellow chain in figure 6.1), with the corresponding group:

Definition 9. *(The Cycle Group)*
Given a simplicial complex K, the group of p-cycles is $Z_p = \{c \in C_p | \partial_p c = 0\}$. Note that this is equivalent to $Z_p = ker\ \partial_p$.

The second group is determined by the boundary. A p-chain $c \in C_p$ is called a p-boundary if there exist a chain $d \in C_{p+1}$ such that $c = \partial_{p+1} d$. An example of a boundary is shown in figure 6.1 in red. The corresponding group is given by:

Definition 10. *(The Boundary Group)*
Given a simplicial complex K, the group of p-boundaries is $B_p = \{c \in C_p | \ \exists \ d \in C_{p+1}$ such that $c = \partial_{p+1} d \ \}$. Note that this is equivalent to $B_p = im \ \partial_{p+1}$.

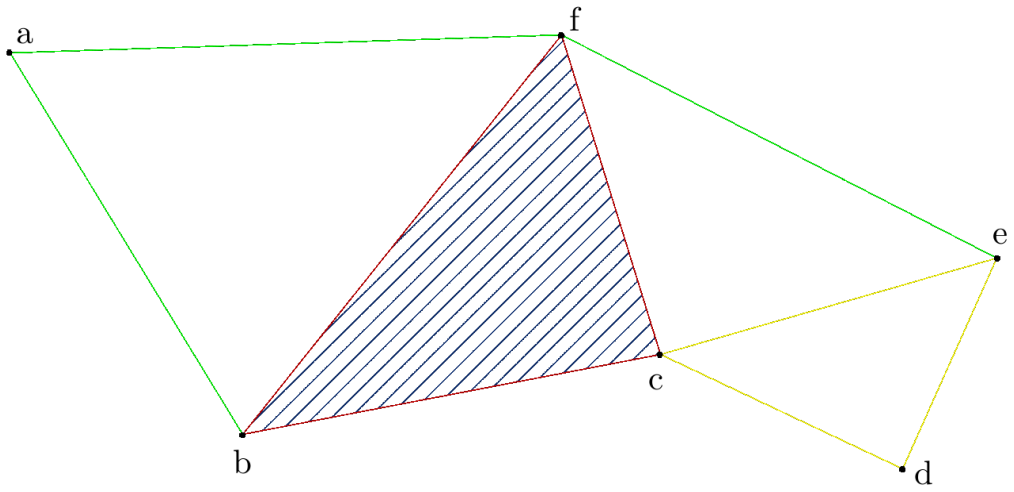

Figure 6.1: This figure shows a simplicial complex. The green elements form a 1-chain, $\sigma_g = ba + af + fe \in C_1$. The yellow elements, $\sigma_y = cd + de + ec \in Z_1$, form a 1-cycle, because their boundary $\partial\sigma_y = c + d + d + e + e + c = 0$. Finally the red elements, $\sigma_r = bc + cf + fb \in B_1$, form a 1-boundary, because for the blue 2-simplex $\sigma_b = bcf$ it holds that $\partial\sigma_b = bc + cf + fb = \sigma_r$.

6.1.4 The Boundary Matrix

In our numerical analysis of the homological structure of Gaussian random fields we use the boundary matrix of a simplicial complex K.

We order the simplices $\{\sigma_1, \ldots, \sigma_n\}$ of a d-dimensional simplicial complex $K = \{\sigma_1, \ldots, \sigma_n\}$ such that for all $i \leq n$, $K_i := \{\sigma_1, \cdots, \sigma_i\}$ is also a simplicial complex. In practice we order the simplices by dimension, where the dimension of σ_i is smaller than the dimension of σ_j for all $i \leq j$. The boundary matrix ∂ of K is an $n \times n$ matrix where the j-th column represents the boundary of σ_j. This means that $\partial_{ij} = 1$ if and only if σ_i is in the boundary of σ_j, and $\partial_{ij} = 0$ if and only if σ_i is not in the boundary of σ_j. Because the dimension of σ_j is larger or equal to the dimension of σ_i for all $i < j$, the matrix ∂ is an upper-triangular matrix.

As an example we calculate the boundary matrix of the figure composed of two triangles shown in figure 6.2. This leads to the following boundary matrix:

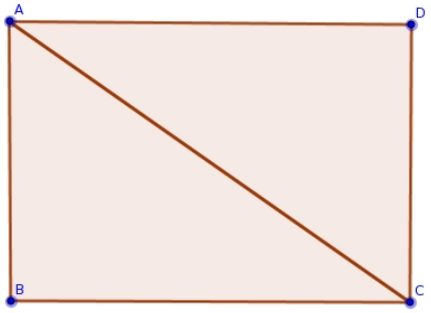

Figure 6.2: A simplicial complex K, consisting of the simplices $\{a, b, c, d, ab, bc, cd, \mathrm{d}a, ac, abc, acd\}$. Its boundary matrix is computed in section 6.1.4

	a	b	c	d	ab	bc	cd	da	ac	abc	acd
a	0	0	0	0	1	0	0	1	1	0	0
b	0	0	0	0	1	1	0	0	0	0	0
c	0	0	0	0	0	1	1	0	1	0	0
d	0	0	0	0	0	0	1	1	0	0	0
ab	0	0	0	0	0	0	0	0	0	1	0
bc	0	0	0	0	0	0	0	0	0	1	0
cd	0	0	0	0	0	0	0	0	0	0	1
da	0	0	0	0	0	0	0	0	0	0	1
ac	0	0	0	0	0	0	0	0	0	1	1
abc	0	0	0	0	0	0	0	0	0	0	0
acd	0	0	0	0	0	0	0	0	0	0	0

As seen from this small example, the boundary matrix becomes very large, even for small and relatively simple simplicial complexes.

6.2 Homology Groups and Betti Numbers

The property that the p-cycles Z_p and the p-boundaries B_p are groups, with $B_p \subset Z_p$, makes it possible to define the p-th homology group.

Definition 11. *(Homology groups)*
Given the cycles Z_p and boundaries B_p of a simplicial complex in p-dimensions, the p-th homology group is defined as $H_p = Z_p/B_p$.

This enables us to define the Betti numbers of a simplicial complex:

Definition 12. *The p-th Betti number is defined as the rank of the p-th homology group. Thus $\beta_p = rank\ H_p$.*

Effectively, the homology group H_p is the cycle group Z_p partitioned in sets which differ by a p-boundary. The homology groups of manifolds such as the torus in figure 6.3 are defined by the homology groups of a triangulation of the torus. The homology groups are independent of the chosen triangulation. [12]

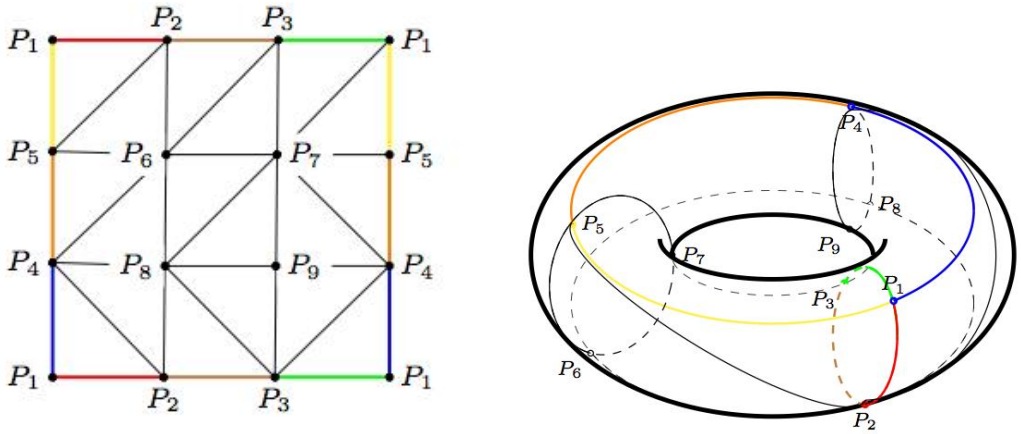

(a) Triangulation of the torus embedded on the plane.

(b) Triangulation of the torus embedded on the torus.

Figure 6.3: A hollow torus has Betti numbers $\beta_0 = 1, \beta_1 = 2, \beta_2 = 1$ [3].

Intuitively, the Betti numbers of the torus are the number of connected parts $\beta_0 = 1$, the number of 1-dimensional open faces $\beta_1 = 2$, and the number of 2-dimensional voids $\beta_2 = 1$.

This is however not a rigorous way to calculate the Betti numbers, the proper way to do it is by using definition 11. This can however become very difficult for relatively simple objects. Fortunately there exists a relatively simple and very useful algorithm to compute Betti numbers. This algorithm is called the incremental algorithm.

6.2.1 Incremental Algorithm for Betti Numbers

In the incremental algorithm one starts with an empty simplicial complex $N_0 = \emptyset$. The Betti numbers of this space are known, $\beta_i = 0$, for $i = 0, 1, 2, \ldots$. Now add a p-simplex σ to N_0 to obtain $N_1 = N_0 \cup \sigma$. Iterating this procedure we can add a p-simplex σ to the simplicial complex N_i, to obtain $N_{i+1} = N_i \cup \sigma$. If $\sigma \in B_p(N_i)$, then $\beta_p \to \beta_p + 1$, if however $\sigma \notin B_p(N_i)$ then $\beta_{p-1} \to \beta_{p-1} - 1$. By iterating this procedure for $i = 1, 2, \ldots$ until N_{i+1} is the desired simplicial complex K, one can compute the Betti numbers of an arbitrary simplicial complex and therefore of an arbitrary object. For a full overview of this algorithm and a simple code to implement it see [10].

6.3 Superlevel Sets

So far we have only examined the homology of static simplicial complexes and manifolds (using triangulations). More information of the topology can be extracted by systematically choosing various subsets of the simplicial complex or manifold and calculating the homology groups for all of the subsets. In order to make sensible subsets we use filtrations, and in particular superlevel sets. A superlevel set is defined as:

Definition 13 (Superlevel set)**.** *Given a function $f : \mathbb{R}^2 \to \mathbb{R}$, we define a 2-dimensional manifold $M \subset \mathbb{R}^3$ by $M = \{(\boldsymbol{x}, f(\boldsymbol{x}))|\boldsymbol{x} \in \mathbb{R}^2\}$. For this manifold M a superlevel set $M(\nu)$ is defined as:*

$$M(\nu) = \{(\boldsymbol{x}, f(\boldsymbol{x})) \in M | f(\boldsymbol{x}) \geq \nu\}.$$

This is obviously a filtration, because $M(\nu) \subseteq M(\mu)$ for all $\nu \geq \mu$.

6.3.1 Betti Numbers

Using superlevel sets we can define the Betti numbers for a nested sequence of subsets of a simplicial complex or manifold. From now on we will call $\beta_p(\nu_0)$ the p-th Betti numbers of the simplicial complex obtained by taking the superlevel set of M at ν_0:

Definition 14. *(Betti numbers)*
Given a manifold M, its Betti numbers are defined as $\beta_p(\nu_0) = rank\ H_p(M(\nu_0))$, where the homology of the manifold $M(\nu_0)$ is equal to the homology of the triangulation of this manifold.

Intuitively, the Betti numbers describe the change in topology of M, while including more and more parts of the object K, as the threshold ν_0 runs from ∞ to $-\infty$. Thus the Betti numbers as a function of the superlevel set value ν_0 form a signature of the homology of the manifold M.

6.4 Alpha Shapes

In order to determine the structure of an n-particle distribution, such as a galaxy distribution, other filtration schemes can be used. One often used filtration method is alpha shapes, which are a subset of a Delaunay triangulation. Alpha shapes are a measure of the topological structure of a point distribution on a scale parametrized by the real number α. They were introduced by Edelsbrunner and Muecke [29, 13] and have since been used to analyze cosmological data by for example van de Weygaert [40]

The alpha complex of a point set P consists of all simplices in the Delaunay triangulation that have a non-empty circumsphere with a radius less than or equal to α. A non-empty circumsphere is defined as a sphere of radius α, centered on a vertex in P that has other vertices of P within its boundary. For example, when α is equal to 0, the alpha complex of P consist of only the vertices in P and when α exceeds a certain value

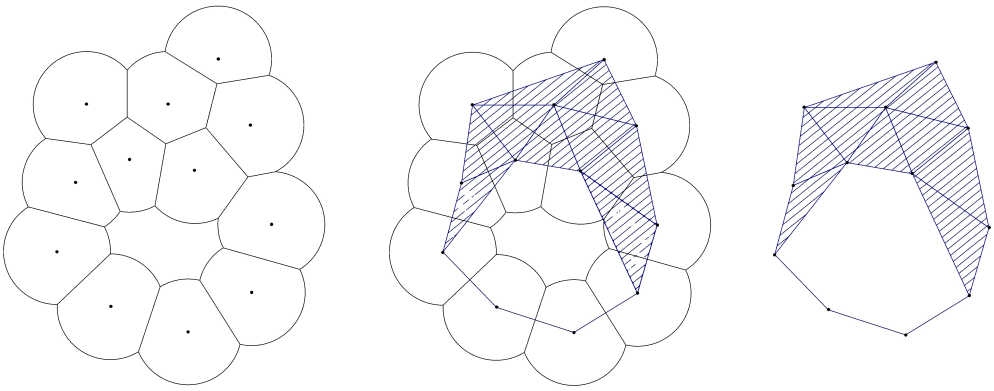

Figure 6.4: This figure shows the construction of the alpha shape of a 2-dimensional point set P for a certain value of α. The left figure shows the point set P, where every point is surrounded by a circle of radius α. The second figure shows how points whose circumcircles intersect are connected. The right figure shows the completed alpha shape of the point set P.

α_{max}, the alpha complex is just the convex hull of P. Using these alpha complexes we define the alpha shape as the union of all simplices in the alpha complex, see figure 6.4 for a 2-dimensional example.

Analogous to the Betti numbers of a superlevel set, Betti numbers can be computed for different filtrations of the Delaunay triangulation. This leads to the possibility of defining the Betti numbers $\beta_i(\alpha)$ as a function of the distance scale α.

Chapter 7

Persistence Diagrams

Persistence Diagrams form a tool to analyze the importance of certain topological features of Gaussian random fields. Starting with an empty superlevel set, and lowering the threshold, structures appear and merge. Intuitively it seems that structures which merge very shortly after they appear are less important for the overall topology of the field, than structures which do not merge for a long time. Persistence diagrams provide a mathematical framework to analyze these structures. Persistence diagrams were introduced by Edelsbrunner, Letcher and Zomorodian [15].

7.1 Persistence of a Simplicial Complex

The method of computing Betti numbers described in section 6.3.1 gives information on the change in homology for different thresholds ν_0. Here we analyze which of these changes in homology are most important. For example: a 1-cycle that is formed at some threshold ν_0 but gets filled by a face at an only slightly lower threshold is of little importance for the overall homological structure of the simplicial complex. However, a 1-cycle that is formed at ν_0, but which does not get closed until a much lower value of ν_0 is passed, is obviously an important feature of the simplicial complex. Persistence diagrams analyze the lifetime of topological features of the simplicial complex for changing filtrations.

As the threshold ν_0 changes from ∞ to $-\infty$, a component appears at a certain threshold and merges with another component at a later threshold. From now on we will call the appearance of a component the *birth* of that component and the merger of a component with a younger component the *death* of that younger component. This is the *Elder rule*, the youngest structure in a merger always dies, while the older structure persists [12].

The birth and death of all components of dimension p, in a simplicial complex K, can be plotted in a persistence diagram. If a p-dimensional structure is born at $\nu_0 = a$ and dies at $\nu_0 = b$, this structure is represented by a point in the persistence diagram P_p at (a, b). Thus a complete persistence diagram is a finite point set, in which every point stands for the birth and death of a p-dimensional structure. In 2 dimensions we will

only be looking at 0-dimensional persistence and 1-dimensional persistence. A simple 1-dimensional example of a graph with its corresponding persistence diagram is shown in figures 7.3d and 7.3e. Note that a structure always has to be born before it dies, and therefore that no points can be below the line $a = b$.

An example of a persistence diagram of a large simplicial complex is shown in figure 7.1. This persistence diagram shows the lifespans of topological features in a Gaussian random field using superlevel sets as the filtration method. A persistence diagram can also be constructed by using a different filtration method, for example alpha shapes. The way in which a simplicial complex is constructed from a Gaussian random field is explained in section 8.2. An important feature of persistence diagrams is that they reflect the structure of the Gaussian random field. It is important to note that most of the points in the persistence diagram are close to the line $a = b$. This implies that nearly all structures die very soon after they are born. This means that in a Gaussian random field, most peaks are surrounded by many other peaks with a similar function value, which is known to be a feature of Gaussian random fields.

The persistence diagram gives us a second method of characterizing the homology groups of a simplicial complex, on top of the Betti numbers. However, the two are not independent.

Theorem 2 (Persistence diagrams and Betti numbers relation)**.** *Given a persistence diagram P_p of a simplicial complex. The Betti number $\beta_p(\nu_0) = \#\{(a, b) \in P_p | b > \nu_0 > a\}$. Where $\#A$ denotes the number of distinct elements in the finite set A. See figure 7.2.*

7.2 Algorithm for Persistence Computation

To compute the persistence diagrams of a simplicial complex we use the reduction algorithm proposed by Edelsbruner, Letscher and Zomorodian [15], and optimized by Chen and Kerber [4].

Edelsbruner et al. [15] use the boundary matrix (see section 6.1.4) of the simplicial complex and reduce it using column operations until every column is either zero or has a unique lowest nonzero element.

We then call any two simplices (σ_i, σ_j) for which the element $\partial_{i,j} \neq 0$ a *persistence pair*. The structure born by inserting the simplex σ_i is killed by the simplex σ_j. Using our method of constructing a simplicial complex described in section 8.2, every simplex has a certain value ascribed to it. We then place a point in the persistence diagram at (a, b), where the value of $\sigma_i = a$ and the value of $\sigma_j = b$. Thus the boundary matrix gives us the full information on the persistence diagram of the simplicial complex constructed on a Gaussian random field.

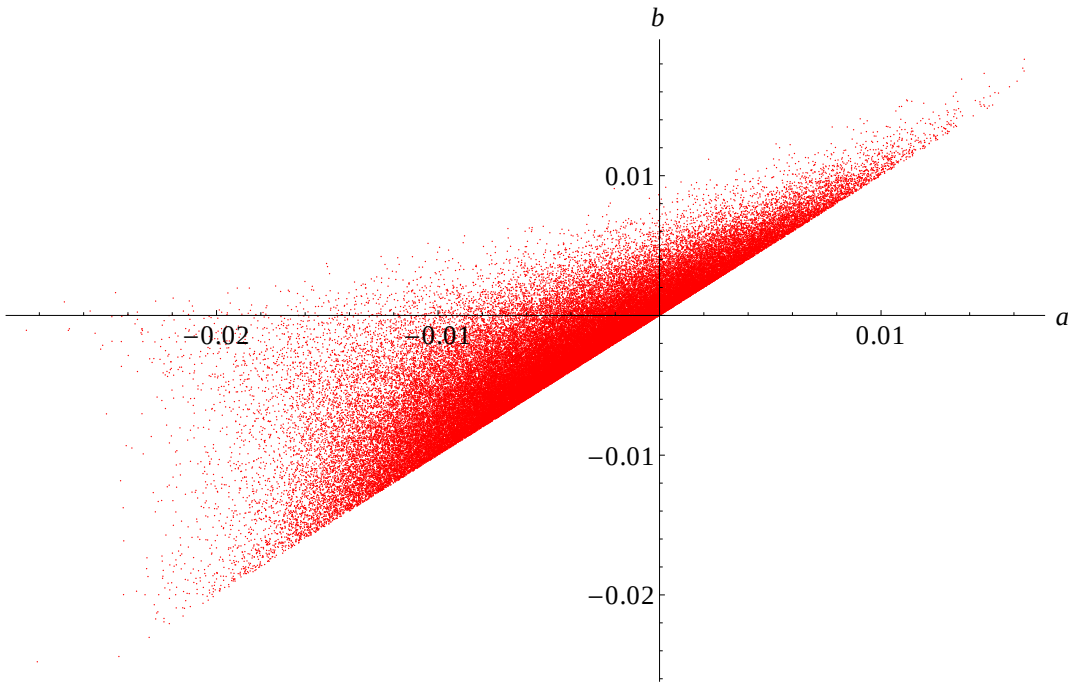

Figure 7.1: An example of a persistence diagram of a simplicial complex. a is the value of ν_0 at which a structure is born, and b is the value of ν_0 at which a structure dies. It can clearly be seen that most structures die soon after they are born. Furthermore, only a limited number of points in the persistence diagram, namely those that are furthest away from the line $a = b$, are showing more important features.

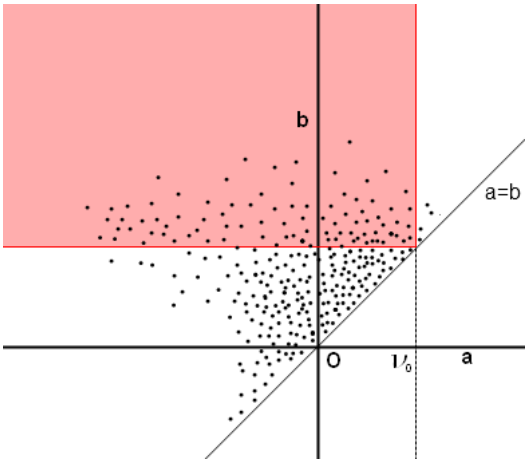

Figure 7.2: The Betti numbers at threshold ν_0 can be calculated from a persistence diagram by summing over the red region.

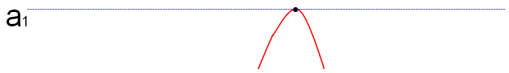

(a) Stage 1: 1 point appears at the threshold a_1.

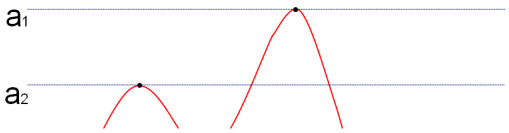

(b) Stage 2: another point appears at threshold a_2.

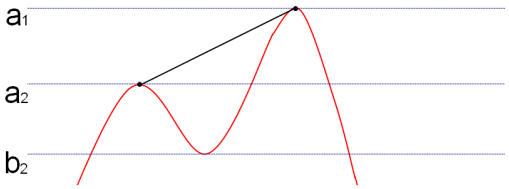

(c) Stage 3: the two points get connected by an edge, appearing at b_2. The structure born at a_2 dies here, since it is younger than the structure born at a_1.

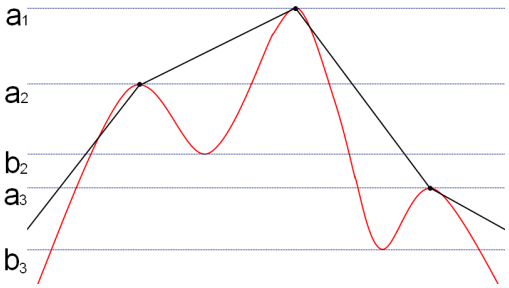

(d) Stage 4: the complete simplicial complex is visible at b_3.

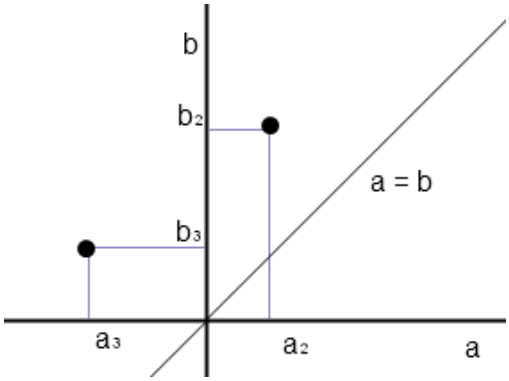

(e) Persistence diagram of the simplicial complexx.

Figure 7.3: By decreasing the threshold from a_1 to b_3, more and more structure of the simplicial complex arises. Using the same principle in a higher dimensional case, we can calculate the Betti numbers of every intermediate step. The 5th figure shows the persistence diagram of this simplicial complex. Only 2 points die in this part of the simplicial complex, the structure born at a_1 never dies. The structure born at a_2 dies at b_2 and the structure born at a_3 dies at b_3, this corresponds to the points (a_2, b_2) and (a_3, b_3) in the persistence diagram.

Part II

Analytical Analysis

Chapter 8

Analytical Predictions of Betti Numbers in Gaussian Random Fields

In this chapter we calculate the Betti numbers of a Gaussian random field. We do this by showing how to apply algebraic topology of simplicial complexes to Gaussian random fields. In order to convert a continuous field to a simplicial complex, we introduce the Morse-Smale complex. In this section we purely deal with analytical predictions of Betti numbers, thus, no realizations are used.

To predict the Betti numbers we postulate formulas which use a probability density function and the critical point densities of the Gaussian random field, as shown in section 5.1. Using these formulas we calculate the expected value of the Betti numbers, and thus do not need any realizations.

8.1 Symmetry of Betti Numbers

The power spectrum of a 2-dimensional Gaussian random field is invariant under multiplication of the field by -1. Under this transformation the maxima transform into minima and vice versa, while the saddle points remain the same. Because, by the incremental algorithm, a maximum always increases β_0 by 1 and a minimum always decreases β_1 by 1, this seems to imply that the Betti numbers obey a symmetry as well. This symmetry is given by:

$$\beta_0(\nu_0) = \beta_1(-\nu_0),$$

and it is formally known as the *Alexander duality* [12].

Because of this symmetry, $\beta_0 : \mathbb{R} \to \mathbb{Z}$ completely characterizes both Betti numbers of a 2-dimensional Gaussian random field. Thus in the coming calculations we will only need to predict β_0. Note that for non-Gaussian fields, the Alexander duality does not apply.

8.2 Constructing a Simplicial Complex from a Gaussian Random Field

To construct a simplicial complex from a realization of a Gaussian random field we use the Morse-Smale complex [14], which is homeomorphic to the field. From this Morse-Smale complex we construct a simplicial complex, which is generically homeomorphic to the Morse-Smale complex.

8.2.1 The Morse-Smale Complex

Given a smooth and compact manifold $\mathbb{M}$, we can define integral lines on $\mathbb{M}$:

Definition 15 (Integral Line)**.** *An integral line $p : \mathbb{R} \to \mathbb{M}$ is a maximal path whose tangent vectors are equal to the gradient, that is $\frac{d}{ds}p(s) = \nabla h(p(s))$, for all $s \in \mathbb{R}$.*

Because of the behavior of Gaussian random fields, which have many critical points, we can be sure that these limits generically exist in Gaussian random fields. Thus we can also define integral lines on Gaussian random fields, which are not necessarily compact.

We will refer to the *origin* of p as $\text{org } p = \lim_{s \to -\infty} p(s)$, and to the *destination* of p as $\text{dest } p = \lim_{s \to \infty} p(s)$. Using these concepts we can define the stable and unstable manifolds of a critical point e:

Definition 16 (Stable and Unstable Manifold)**.**
Stable manifold: $S(e) = \{p | \textit{dest } p = e\} \cup \{e\}$,
Unstable manifold: $U(e) = \{p | \textit{org } p = e\} \cup \{e\}$.

In terms of the stable and unstable manifold, we define the Morse-Smale cells as the intersections between the stable and the unstable manifold. The Morse-Smale cells are the connected components of the set $U(e_1) \cap S(e_2)$ for all critical points $e_1, e_2 \in \mathbb{M}$. The Morse-Smale complex is then the collection of all Morse-Smale cells, see Figure 8.1a for an example.

8.2.2 Creating a Simplicial Complex

To create a simplicial complex from this Morse-Smale complex we replace every maximum by a vertex. Besides the ordinary properties of the vertex we also assign a number to it, given by the value of the field at the location of the maximum. Furthermore we replace every saddle point by an edge. This edge connects the two vertices associated with the maxima connected by the integral line in the Morse-Smale complex. To this edge we assign the value of the field in the corresponding saddle point. Finally we replace every minimum by a face, the boundary of which is given by the edges constructed by the saddle points connected to the minimum. We a associate a value with this face corresponding to the value of the field at the minimum. The simplicial complex obtained from the Morse-Smale complex shown in figure 8.1a is shown in figure 8.1b. Note that a maximum which is connected to only one other maximum is a non-generic case. In the conversion from a Morse-Smale complex to a simplicial complex we choose to ignore

those maxima. One of those maxima can be seen in 8.1a, surrounded by bold lines.

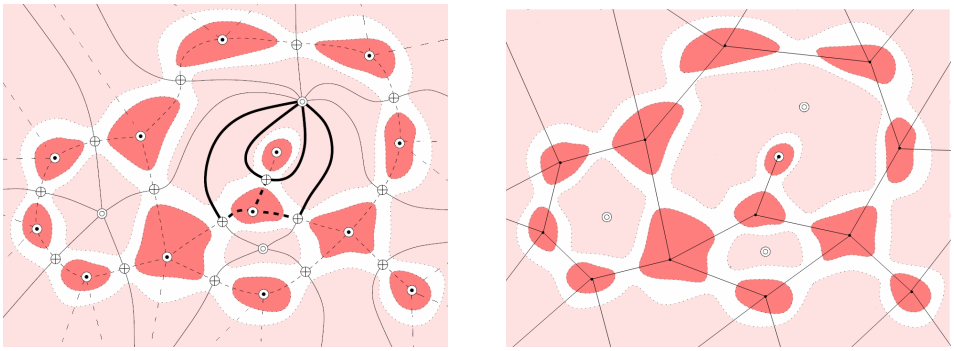

(a) A Morse-Smale complex [14] (b) A simplicial complex

Figure 8.1: Here $\odot, \oplus$ and $\circledcirc$ represent maxima, saddle points and minima. Apart from the non-generic cases, this simplicial complex is homeomorphic to the Morse-Smale complex and therefore also to the Gaussian random field.

8.3 Calculating Betti Numbers for Gaussian Random Fields

In order to compute the Betti numbers of superlevel sets of Gaussian random fields, we use the incremental algorithm defined in section 6.2.1. β_0 and β_1 of a realization are shown in figure 8.2. For very high thresholds ν_0 all points $\mathbf{r} \in \mathbb{R}^2$ obey $f(\mathbf{r}) < \nu_0$; this corresponds to an empty simplicial complex. While ν_0 decreases, more and more points of the field get added to the superlevel set. This corresponds to the addition of the simplices with an assigned value larger than ν_0 to the simplicial complex.

When ν_0 decreases, the amount of added maxima above the threshold ν_0 corresponds to the amount of vertices added to the simplicial complex. According to the incremental algorithm, this corresponds to β_0 increasing by 1. Similarly, an additional saddle point appearing above the threshold, corresponds to the addition of an edge to the simplicial complex. This implies that either β_0 goes down by 1 or that β_1 goes up by 1. Finally, the addition of a minimum corresponds to the addition of a face, which either reduces β_1 by 1 or increases β_2 by 1. This process, implied by the incremental algorithm, is represented in table 8.1. An increase in β_2 in a 2-dimensional case will only happen when the lowest minimum is added to the simplicial complex, it has only been added to the table for completion.

In our analytical analysis, we do not work with any realizations of Gaussian random fields. Therefore we do not construct any specific simplicial complexes. Instead, given a Gaussian random field (defined by its power spectrum) $f : \mathbb{R}^2 \to \mathbb{R}$ we calculate the

critical point of index n	β_0	β_1	β_2	added components
0	$\uparrow$			an isolated vertex
1	$\downarrow$	$\uparrow$		an edge
2		$\downarrow$	$\uparrow$	a face

Table 8.1: Influence of critical points on the Betti numbers of a simplicial complex

statistically predicted expected values of the Betti numbers. To do this density of maxima $\mathcal{N}_0(\nu)$, saddle points $\mathcal{N}_1(\nu)$, and minima $\mathcal{N}_2(\nu)$ in a 2-dimensional field, derived in section 5.1. Note that the indices of the density functions correspond to the indices of the critical points (the number of positive eigenvalues of its Hessian).

Using table 8.1 we can define the following relation between the critical points and Betti numbers of a Gaussian random field:

$$\beta_0(\nu_0) = \int_{\nu_0}^{\infty} [\mathcal{N}_0(\nu) - (1 - g(\nu))\mathcal{N}_1(\nu)]d\nu \tag{8.1}$$

$$\beta_1(\nu_0) = \int_{\nu_0}^{\infty} [g(\nu)\mathcal{N}_1(\nu) - \mathcal{N}_2(\nu)]d\nu. \tag{8.2}$$

Here $g(\nu)$ is the probability that an added saddle point at threshold ν, and corresponding edge, increases β_1 by 1. This means that it is the probability that the edge added by the saddle point forms a cycle.

8.4 Calculating $g(\nu)$

In order to investigate the behavior of the function $g : \mathbb{R} \to [0, 1]$ is, we consider limit cases. First we consider the cases where the threshold ν goes to infinity or to minus infinity.

For ν_0 sufficiently large, β_1 will go to 0, since there will be no saddle points above a certain threshold. Without saddle points, no cycles have been formed yet, while there are maxima above the threshold already. Thus $\beta_0(\nu_0) \gg \beta_1(\nu_0)$ at high values of ν_0. Similarly, for ν_0 sufficiently negative, β_0 will go to 0, since every single maximum will be connected to every other maximum below a certain threshold. At this threshold, cycles will still exist, and thus $\beta_1(\nu_0) \gg \beta_0(\nu_0)$.

Using relations 8.1 and 8.2 we can approximate $g(\nu)$ when ν is sufficiently large or sufficiently negative. Furthermore, because of the symmetry of Gaussian random fields, it follows that $g(0) = \frac{1}{2}$. Thus the nature of Gaussian random fields combined with

equations 8.1 and 8.2 imply that $g(\nu)$ can be approximated by:

$$g(\nu \text{ large}) \approx \frac{\mathcal{N}_2(\nu)}{\mathcal{N}_1(\nu)} \tag{8.3}$$

$$g(\nu \text{ large negative}) \approx 1 - \frac{\mathcal{N}_0(\nu)}{\mathcal{N}_1(\nu)}, \tag{8.4}$$

$$g(\nu = 0) = \frac{1}{2} \tag{8.5}$$

Using these limit cases of $g(\nu)$ we have constructed a fitting formula:

$$g(\nu) \approx \frac{e^{-\alpha\nu}(1 - \frac{\mathcal{N}_0(\nu)}{\mathcal{N}_1(\nu)}) + e^{\alpha\nu}\frac{\mathcal{N}_2(\nu)}{\mathcal{N}_1(\nu)}}{e^{\alpha\nu} + e^{-\alpha\nu}}, \tag{8.6}$$

where α is a fine-tuning parameter. See figure 8.3 for a plot of $g(\nu)$.

Using this fit in equations 8.1 and 8.2 we obtain the Betti numbers in figure 8.2. Here the red and blue curves of β_1 respectivily β_0 are data obtained with numerical methods using realizations of a Gaussian random field. The black dots are the Betti numbers predicted by equations 8.1, 8.2 and 8.6. The Betti numbers are very dependent on the behavior of $g(\nu)$. That this fit predicts the Betti numbers so well is a good indication that the formula we found for $g(\nu)$ is appropriate.

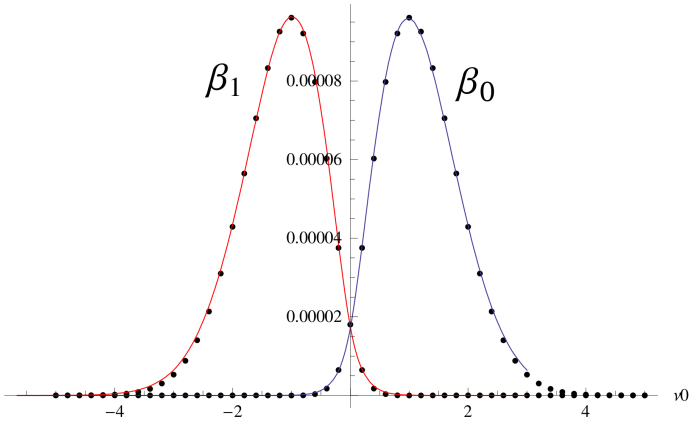

Figure 8.2: Comparison of numerically obtained Betti numbers (β_0 blue and β_1 red) and analytical predictions using $g(\nu)$ according to equations 8.1, 8.2 and 8.6 with $\alpha = 2.7$ (black dots).

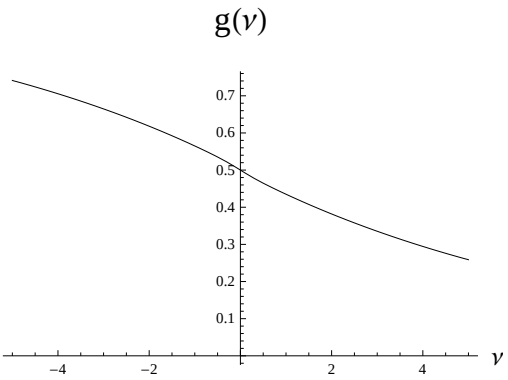

(a) The function $g(\nu)$.

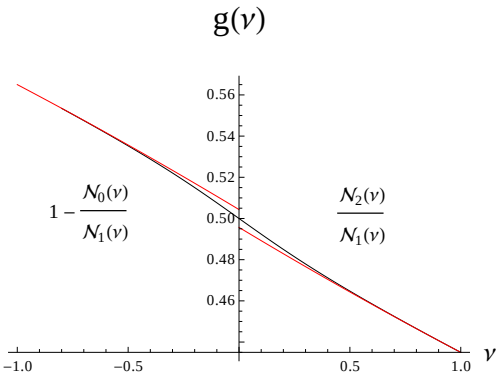

(b) The function $g(\nu)$ approximating its limit cases.

Figure 8.3: This figure shows the function $g(\nu)$, and how well it approximates its limiting cases, obtained from equations 8.1 and 8.2 using $\alpha = 2.7$.

Chapter 9

Analytical Prediction of Persistence Diagrams of Random Gaussian Fields

In the previous chapter we proposed a method of analytically predicting Betti numbers. In this chapter we propose a method of analytically predicting persistence diagrams. As in the previous section, we are not interested in the persistence diagram of realizations of Gaussian random fields, rather we are interested in the statistically predicted expected persistence diagrams.

9.1 Symmetry of Persistence Diagrams

Using the same properties of Gaussian random fields as in section 8.1, we can derive an analogous symmetry for persistence diagrams. This turns out to be:

$$P_0(a, b) = P_1(-b, -a). \tag{9.1}$$

Due to this symmetry we only concentrate on finding an expression for $P_0(a, b)$. Note that in the presence of non-gaussian deviations, symmetry breaking occurs.

9.2 Independence of Birth and Death

Persistence diagrams encode the birth and death of features in Gaussian random fields. First we construct persistence diagrams on the assumption that the threshold at which a feature dies, b, is independent of the threshold a at which the feature is born. Assuming this independence, we use the incremental algorithm in combination with $g(\nu)$ to directly calculate persistence diagrams from the expected values of maxima, saddle points and minima of Gaussian random fields. Under this assumption, the formulas for 0-dimensional and 1-dimensional persistence in a 2-dimensional Gaussian random field

are given by:

$$P_0(a,b) = P(\text{birth} = a \text{ and death} = b \text{ of a 0-structure}) \tag{9.2}$$
$$= \mathcal{N}_0(a)\mathcal{N}_1(b)(1-g(b)) \tag{9.3}$$
$$P_1(a,b) = P(\text{birth} = a \text{ and death} = b \text{ of a 1-structure}) \tag{9.4}$$
$$= \mathcal{N}_1(a)\mathcal{N}_2(b)g(b). \tag{9.5}$$

These are the expression for the persistence diagrams assuming that the expressions 8.1 and 8.2 are correct.Computing the Betti numbers from the persistence diagrams used with the above expressions does in fact yield the Betti numbers as predicted by equations 8.1 and 8.2. Using these formulas for the persistence diagrams, we obtain the persistence diagrams depicted in figure 9.1.

Note that this prediction is a probability distribution that gives the probability that an individual point (a, b) appears in a persistence diagram of a realization. This prediction has the same general characteristics as persistence diagrams of an realization. For more precise predictions the independence between birth and death is not valid.

9.3 Dependence of Birth and Death

9.3.1 Calculating Local Persistence

Although the independence of birth and death seems to be a good first approximation, a more precise prediction requires the correlation of maxima and saddle points. To incorporate this dependence into the predicted persistence diagrams we need to derive the probability that a structure which is born at a dies at b. Because of the symmetry of persistence diagrams we will only consider 0-dimensional structures which are born by a maximum and killed by a saddle point.

The distribution of saddle points at height b, constrained to a maximum at height a, can only be calculated by specifying the distance x by which the maximum is separated from the saddle point (see figure 5.4). This distribution is given by $p_{12}(a, b, x)$, here denoted as $p_0(a, b, x)$, and called *local persistence*, which was derived in section 5.6. We show some of the resulting plots in figure 9.2. Here we use a set value of x in each plot and then plot all points a and b and their corresponding local persistence $p_0(a, b, x)$.

Several observations can be made:

1. The larger the threshold difference between a and b, the smaller $p_0(a, b, x)$ becomes. This simply means that there is only a very small correlation between critical points with very different function values.

2. The limit of $p_0(a, b, x)$ as $x \to \infty$ is simply the $P_0(a, b)$ we obtained in section 9.2. This is because if a peak and a saddle point are very far from each other, there is little correlation between the two critical points.

3. Regardless of the distance between the peak and the saddle point, there is a high density of saddle points which have a function value close to that of the maximum.

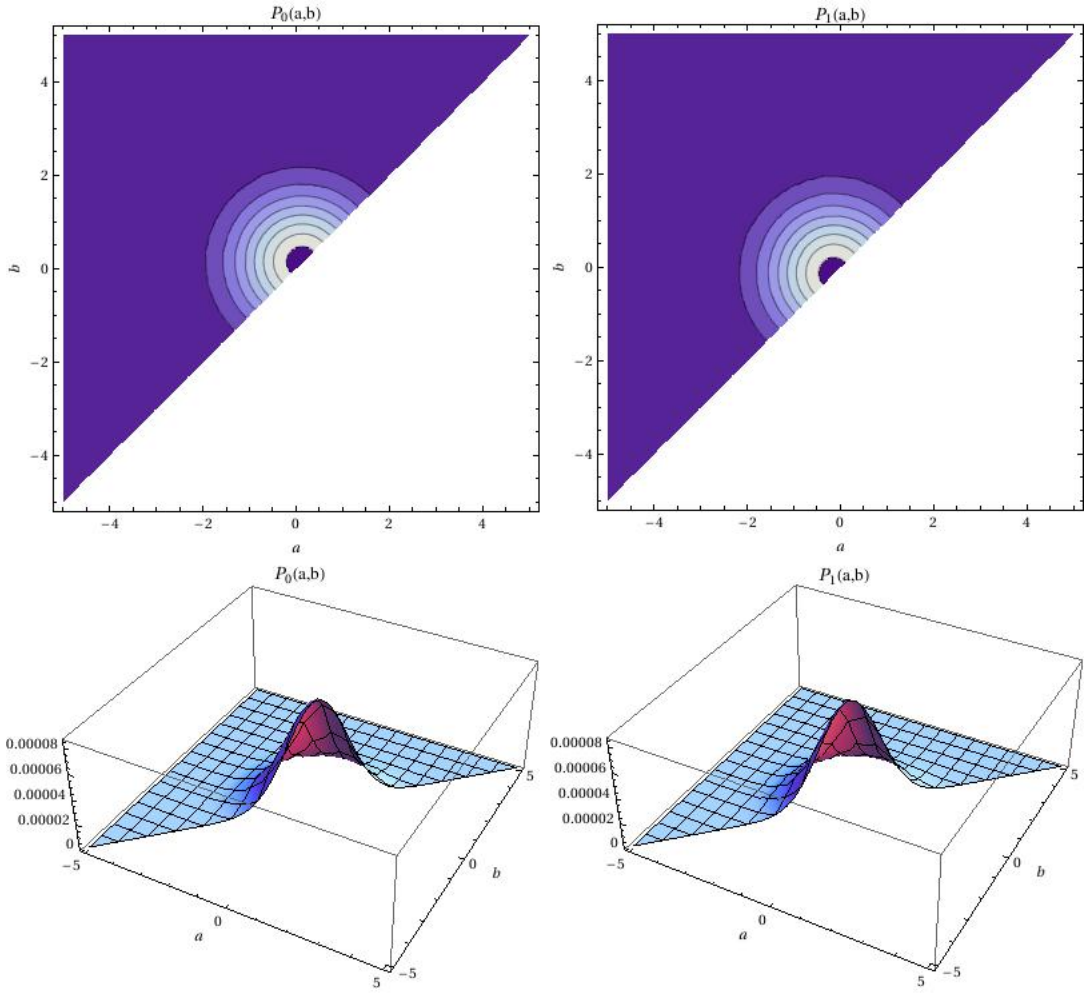

Figure 9.1: Predicted persistence diagrams, assuming independence between birth and death. The plots in the top row are contour plots of $P_0(a, b)$ and $P_1(a, b)$, while the bottom row are the same functions plotted in 3D.

Saddle points which have a much lower function value than the maximum are less dense.

4. When x is small, the density of saddle points with a much lower function value is very low. As x gets larger the density of saddle points at lower function values increases. This can be seen by the graph flattening out as x gets larger.

9.3.2 Combining Local Persistence

To obtain the complete persistence diagram, we need to combine the local persistence functions for different a, b and x. Every local persistence function will have a contribution to the complete persistence diagram, weighted by the probability that the saddle point at height b will kill the maximum at height a, separated by a distance x. This leads to a weighted average of the local persistence functions. We call this weight function $Q : \mathbb{R}^2 \times \mathbb{R}^+ \to [0, 1]$. The function Q is dependent on a, b and x. This leads to the following analytical prediction for the complete persistence $P_i(a, b)$:

$$P_i(a, b) = \int_0^\infty Q_i(a, b, x) p_i(a, b, x) dx, \tag{9.6}$$

where i stands for the i-dimensional persistence.

From this equation the Betti numbers can be derived using theorem 2 and the symmetry of persistence given in equation 9.1:

$$\beta_i = \int_{-\infty}^{\nu_0} \int_{\nu_0}^{\infty} P_i(a, b) \mathrm{d}a\mathrm{d}b = \int_{-\infty}^{\nu_0} \int_{\nu_0}^{\infty} \int_0^\infty Q_i(a, b, x) p_i(a, b, x) \mathrm{d}x\mathrm{d}a\mathrm{d}b \tag{9.7}$$

We have not been able to find an expression for Q_0 yet, but we are able to pose some constraints on this function. First of all, the function Q_0 must exist, since it is the probability density function which specifies whether a saddle point at threshold b forms a cycle when connected to a maximum at threshold a a distance x away from the saddle point. Using this interpretation of $Q_0(a, b, x)$, it can easily be seen that $Q_0(a, b, x)$ is the local analogue of $g(\nu)$ as obtained in section 8.4. Using similar integration intervals as for the computation of Betti numbers from the persistence diagram, $Q_0(a, b, x)$ must obey:

$$g(\nu) = \int_0^\infty \int_{-\infty}^{\nu} \int_{\nu}^{\infty} Q_0(a, b, x) \mathrm{d}a\mathrm{d}b\mathrm{d}x. \tag{9.8}$$

Another promising constraint on $Q_0(a, b, x)$ can be found by linking it to the Euler characteristic. It can be shown that the oscillating sum of the Betti numbers is equal

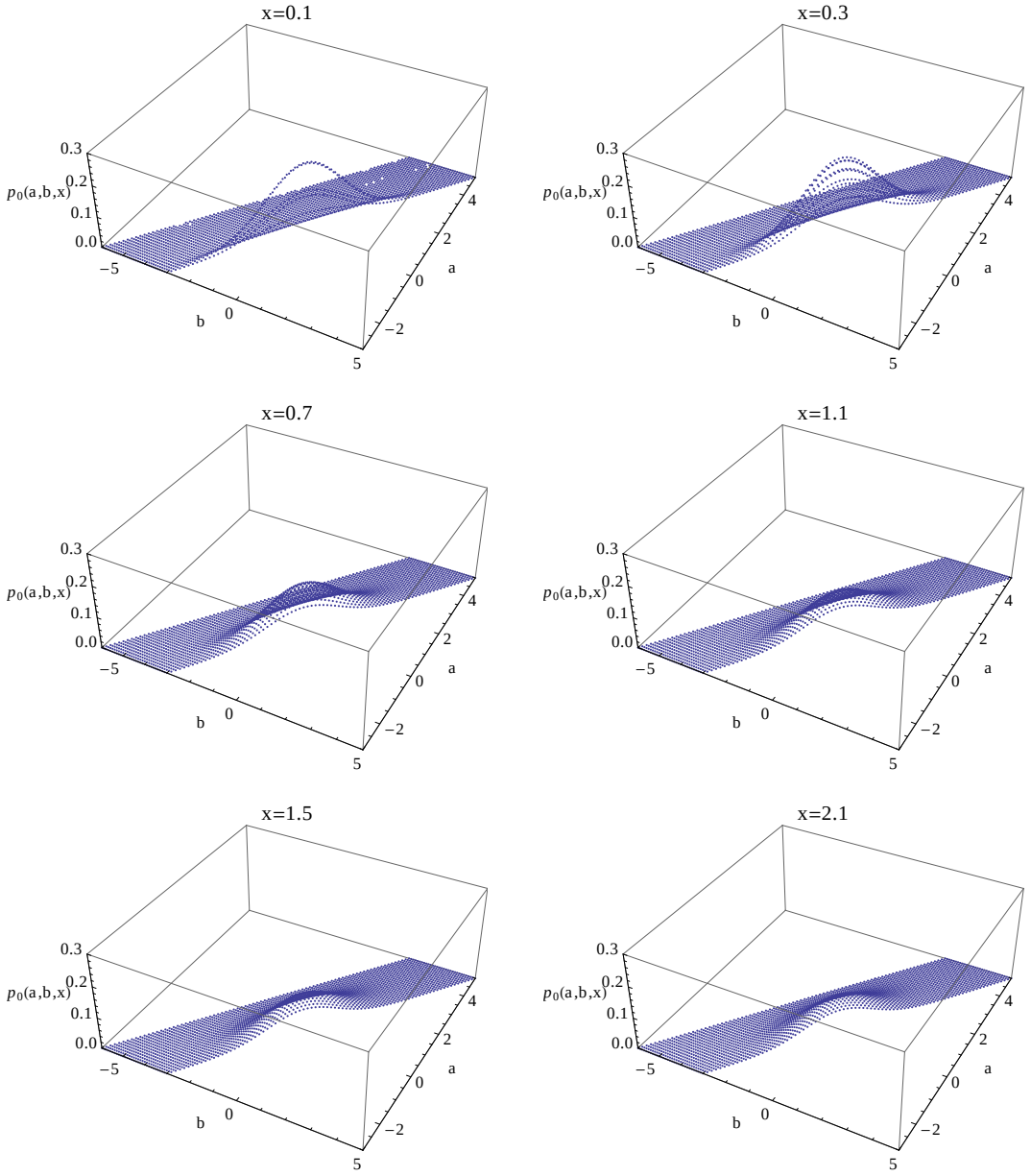

Figure 9.2: Local persistence is shown for different values of x, the distance between a peak a and a saddle point b

to the Euler characteristic $\chi = \beta_0 - \beta_1$. For superlevel set filtrations of a 2-dimensional Gaussian random fields the Euler characteristic is known to be [16]:

$$\chi = (2\pi)^{-3/2} \frac{\langle k^2 \rangle}{2} \nu e^{\frac{-\nu^2}{2}}.$$

We can then use equation 9.7 to link local persistence and Q_0 to the Euler characteristic. We obtain the following relation:

$$\chi = (2\pi)^{-3/2} \cdot \frac{\langle k^2 \rangle}{2} \exp(\frac{-\nu^2}{2})\nu = \int_{\nu_0}^{\infty} \int_{-\infty}^{\nu_0} \big[P_0(a,b) - P_1(a,b)\big] \mathrm{d}a\mathrm{d}b. \tag{9.9}$$

We can now use relation 9.6 and after that relation 9.1 to obtain:

$$\begin{aligned} &(2\pi)^{-3/2} \cdot \frac{\langle k^2 \rangle}{2} \exp(\frac{-\nu^2}{2})\nu \\ &\quad = \int_{\nu}^{\infty} \int_{-\infty}^{\nu} \int_{0}^{\infty} \Big[Q_0(a,b,x) p_0(a,b,x) - Q_0(-b,-a,x) p_0(-b,-a,x) \Big] \mathrm{d}x\mathrm{d}a\mathrm{d}b. \end{aligned}$$

The only unknown quantity in this equation is Q_0, and this formula might lead to other hints about the character of Q_0.

Part III

Numerical Analysis

Chapter 10

Numerical Persistence Diagrams

In the previous part Betti numbers and persistence diagrams of Gaussian random fields were analyzed using an analytical approach. In this chapter we probe the sensitivity of persistence diagrams to non-Gaussianities using numerical calculations. The realizations of Gaussian random fields are produced using the method described in section 4.1.4. So far we have only been able to produce local non-Gaussianities. Local non-Gaussianities are added to the Gaussian random field by using the definition of local non-Gaussianities, see section 2.4.1:

$$\Phi^{NG} = \Phi^{G} + f_{NL}\bigg((\Phi^{G})^2 - \langle\Phi^{G}\rangle^2\bigg), \tag{10.1}$$

where Φ^{NG} is the non-Gaussian field and Φ^{G} is the original realization to which the non-Gaussianities are added. Note that the power spectrum of Φ^{NG} is identical to the power spectrum of Φ^{G}, while Φ^{NG} contains higher order correlation functions differing form the correlation functions predicted by Isserlis's theorem [42, 41].

We have constructed Gaussian random fields with several different power spectra. In the following two sections we first analyze the persistence diagrams of a Gaussian random field with the power spectrum introduced by Bardeen et al. [19] as a realistic approximation of the ΛCDM universe 2.2.1. In the second section we consider a power law power spectrum to probe the general behavior of non-Gaussianities in persistence diagrams.

10.1 Non-Gaussianities in GRFs with a BBKS Power Spectrum

Recall from section 2.2.1 that the BBKS power spectrum is given by:

$$P(k) = k^n T^2(k),\ T(k) = \frac{\log(1+2.34q)}{2.34q}[1+3.89q+(16.1q)^2+(5.4q)^3+(6.71q)^4]^{-1/4},$$

where $q = k/(\Omega_0 h^2\ Mpc^{-1})$. In our realizations we have used $n = 1$.

We have made multiple realizations of Gaussian random fields with this power spectrum and imposed non-Gaussianities on those functions using equation 10.1. For the

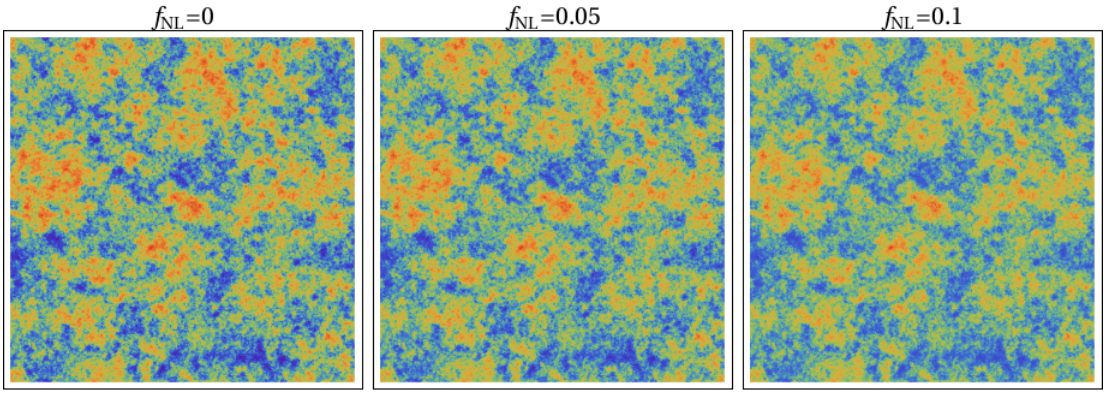

Figure 10.1: A Gaussian random field with a BBKS power spectrum without non-Gaussianities is shown on the left. The right two plots are the same Gaussian random field but with non-Gaussianities imposed using equation 10.1. The middle plot has less non-Gaussianities than the right plot.

effect of those non-Gaussianities on the Gaussian random field, see figure 10.1, which shows both the Gaussian and two non-Gaussian fields.

The 0-dimensional persistence diagrams for these realizations, along with some realizations with intermediate values of f_{NL}, are shown in figure 10.2. Several observations can be made:

1. The points in the persistence diagram generally move to the right in the persistence diagram, thus showing that the maxima of the Gaussian random field become higher and more diffused than the minima as f_{NL} increases.

2. The persistence diagram flattens out towards the line $a = b$ as f_{NL} increases. Thus, as the strength of non-Gaussianities increases, features in the Gaussian random field become shorter lived.

3. In the left part of the persistence diagram a complex change in the shape of the persistence diagram occurs while the strength of non-Gaussianities increases. This implicates that the effect of local non-Gaussianities on 0-dimensional persistence is more prominent at low thresholds.

Further research is required to analyze the behavior of persistence diagrams of Gaussian random fields with a BBKS power spectrum under the influence of non-Gaussianities in more detail. Different types of non-Gaussianities will have to be imposed on the Gaussian random field. However, figure 10.2 shows that persistence diagrams are a promising approach to analyzing non-Gaussianities in Gaussian random fields.

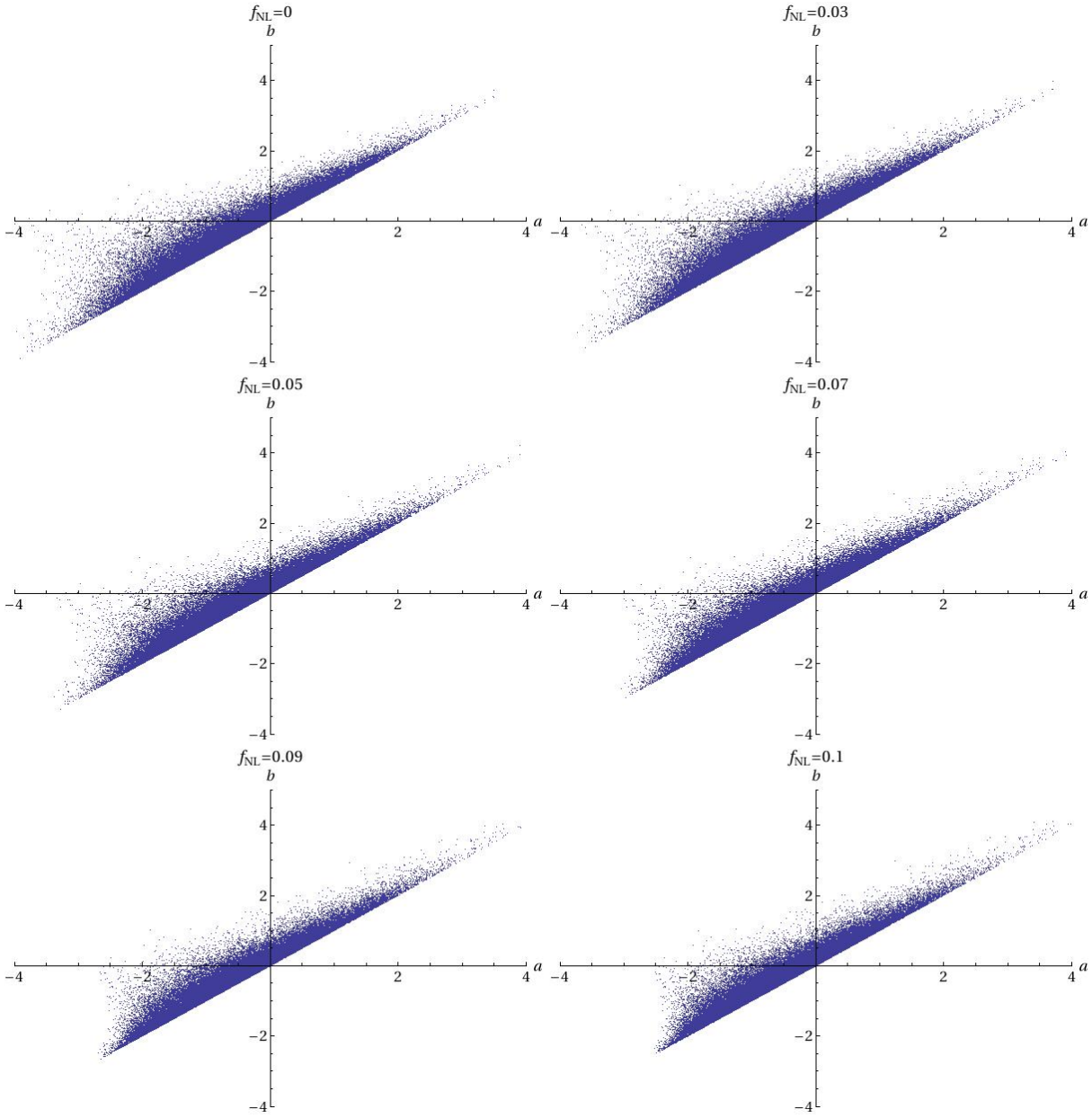

Figure 10.2: The top left figure shows the 0-dimensional persistence diagram of a realization of a Gaussian random field with a BBKS power spectrum. The other figures show the 0−-dimensional persistence diagrams of the field with local non-Gaussianities imposed. It can be seen that the shape of the persistence diagram changes significantly as a function of the strength of non-Gaussianity f_{NL}.

10.2 Non-Gaussianities in GRFs with Power Law Power Spectrum

In this section we turn to a power law power spectrum which gives a good insight in the effect of non-Gaussianities on persistence diagrams. The power law power spectrum is given by:

$$P(k) = A_0 k^{n_s},$$

where A_0 is a normalization constant.

We have made realizations of Gaussian random fields with this power spectrum for $n_s = 0$, $n_s = -1$ and $n_s = -2$. We have then imposed various amounts of non-Gaussianities. Plots of the Gaussian random field and the non-Gaussian fields are shown in figure 10.3.

The 0-dimensional persistence diagrams of these Gaussian random fields and their non-Gaussian versions are shown in figures 10.4, 10.5 and 10.6 for $n_s = 0$, $n_s = -1$ and $n_s = -2$ respectively. Again several observations can be made:

1. As in the BBKS power spectrum case, the points in the persistence diagram generally move to the right in the persistence diagram, thus showing that the maxima of the Gaussian random field become higher and more diffused than the minima as f_{NL} increases.

2. The persistence diagrams flatten out towards the line $a = b$ as f_{NL} increases. This was also seen in the BBKS case.

3. In the left part of the persistence diagram a complex change in the shape of the persistence diagram occurs while the strength of non-Gaussianities increases. This implicates that the effect of local non-Gaussianities on 0-dimensional persistence is more prominent at low thresholds.

4. A significant difference can be seen between the persistence diagrams for the different values of n_s.

5. A difference can be seen between the persistence diagrams of a Gaussian random field with a BBKS power spectrum and fields with a power law power spectrum.

These results indicate once more that persistence diagrams are very sensitive to changes in Gaussian random fields. When changing the power spectrum or when imposing non-Gaussianities, significant changes can be seen in the resulting persistence diagrams. Although more powerspectra and especially more types of non-Gaussianities need to be analyzed, the results shown in this section reinforce the idea that persistence diagrams could be a major tool in analyzing the CMB.

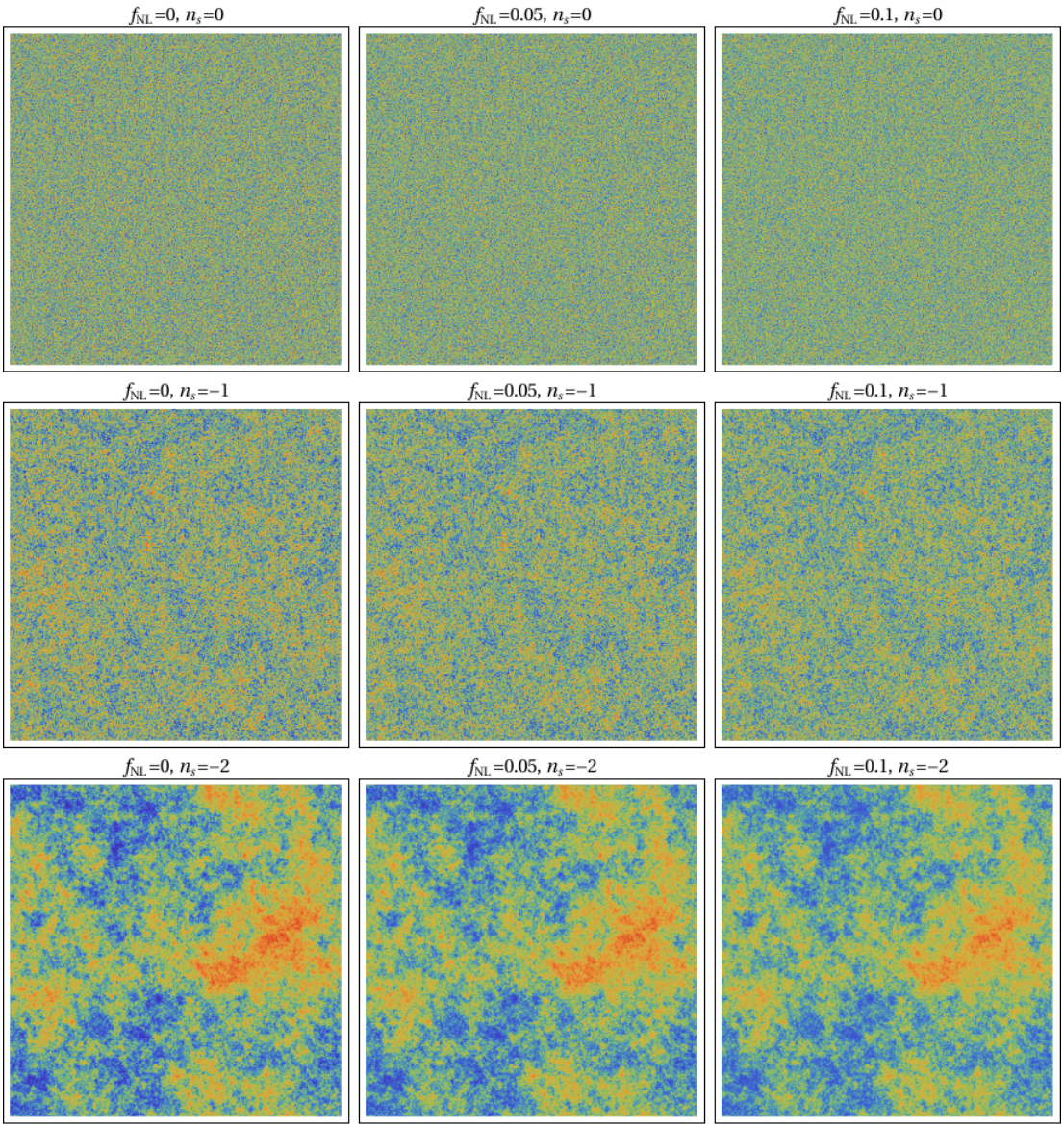

Figure 10.3: Gaussian random fields with a power law power spectrum with values of $n = 0, -1, -2$ are shown. The left column consists of plots of the Gaussian random field, while the right two columns consist of the same fields but with different amounts of local non-Gaussianities imposed.

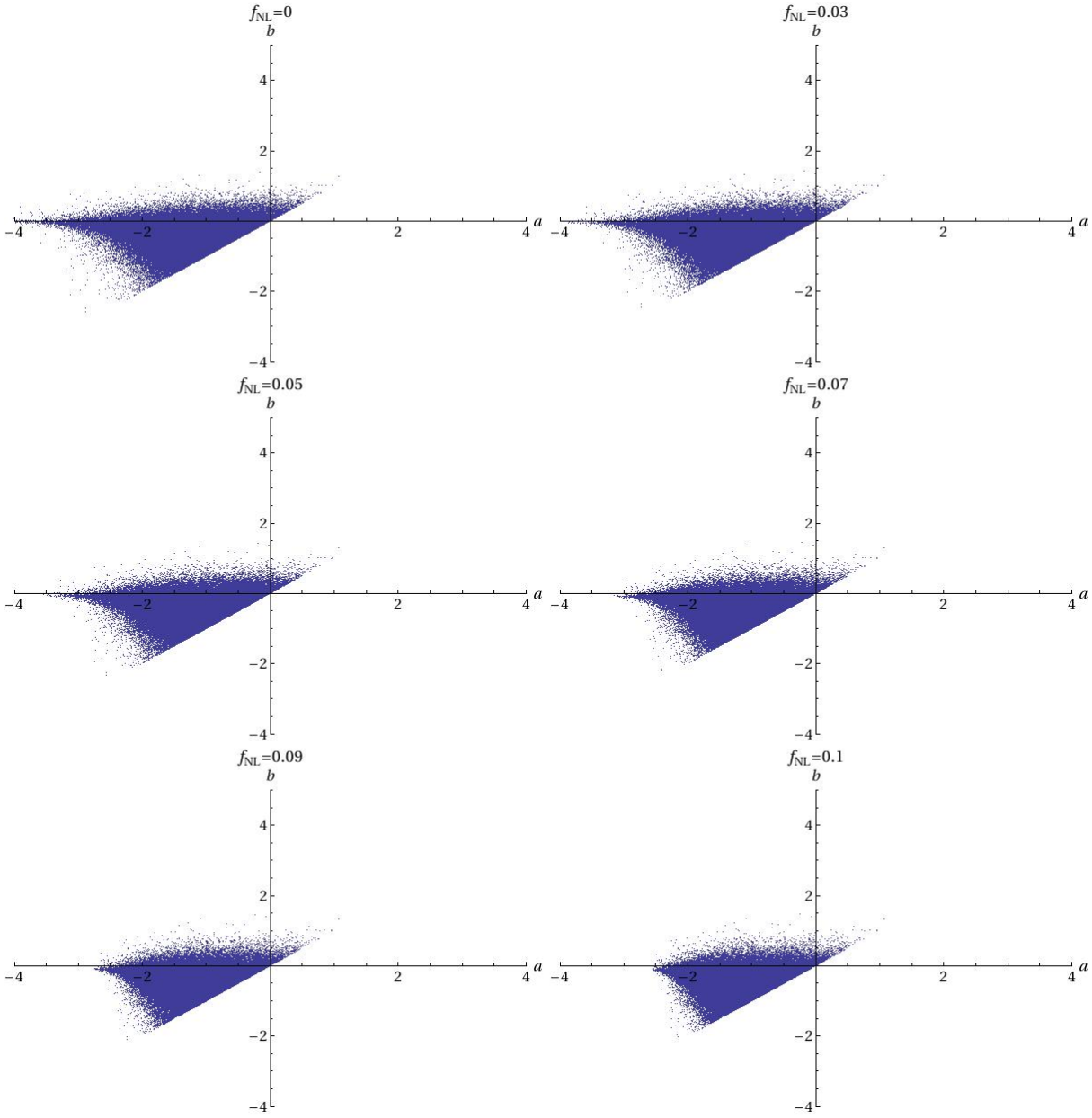

Figure 10.4: The top left figure shows the 0-dimensional persistence diagram of a realization of a Gaussian random field with a power law power spectrum with $n_s = 0$. This is thus a white noise field. The other figures show the 0−-dimensional persistence diagrams of the field with local non-Gaussianities imposed. It can be seen that the shape of the persistence diagram changes significantly as a function of the strength of non-Gaussianity f_{NL}.

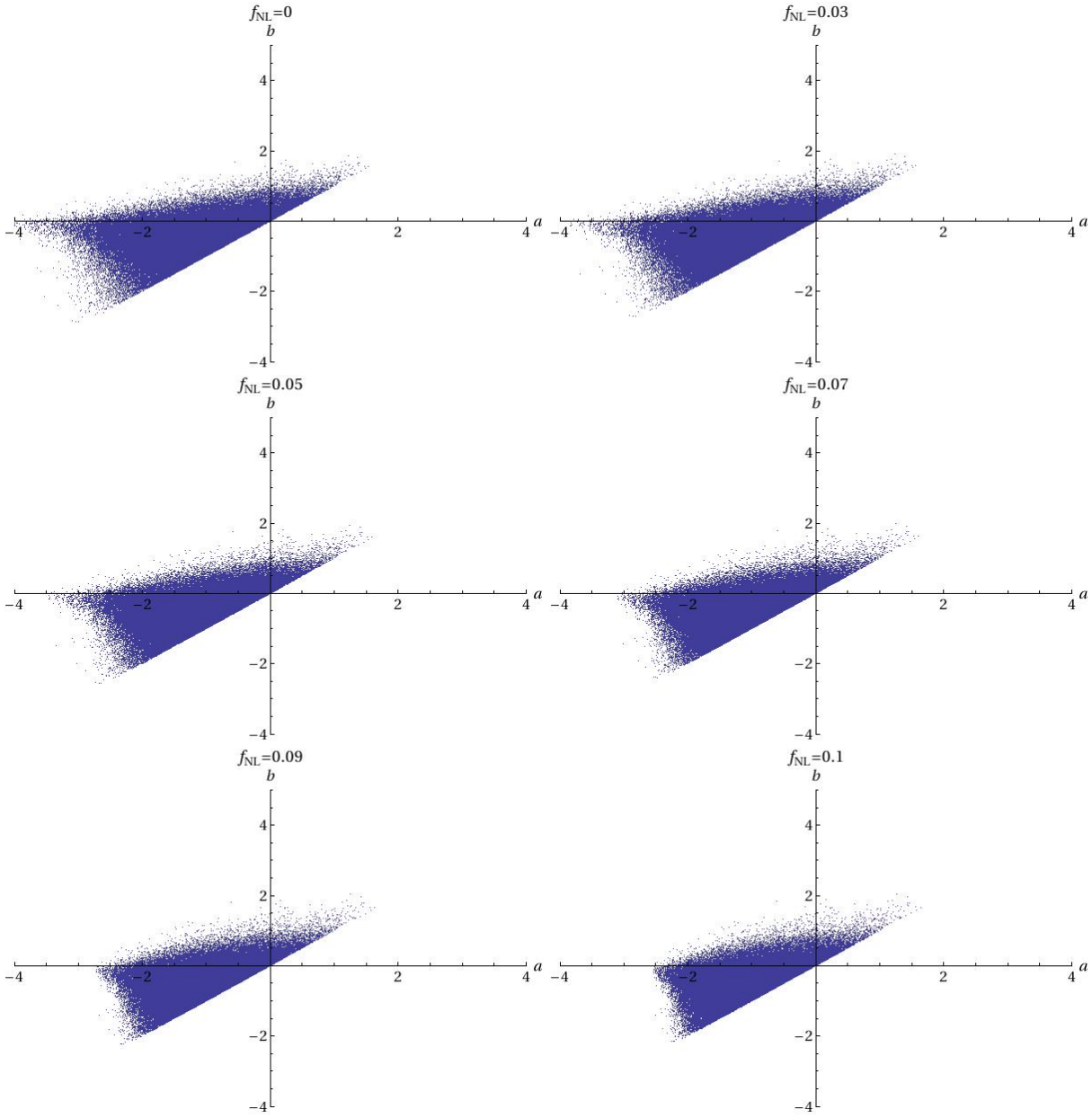

Figure 10.5: The top left figure shows the 0-dimensional persistence diagram of a realization of a Gaussian random field with a power law power spectrum with $n_s = -1$. The other figures show the 0−-dimensional persistence diagrams of the field with local non-Gaussianities imposed. It can be seen that the shape of the persistence diagram changes significantly as a function of the strength of non-Gaussianity f_{NL}.

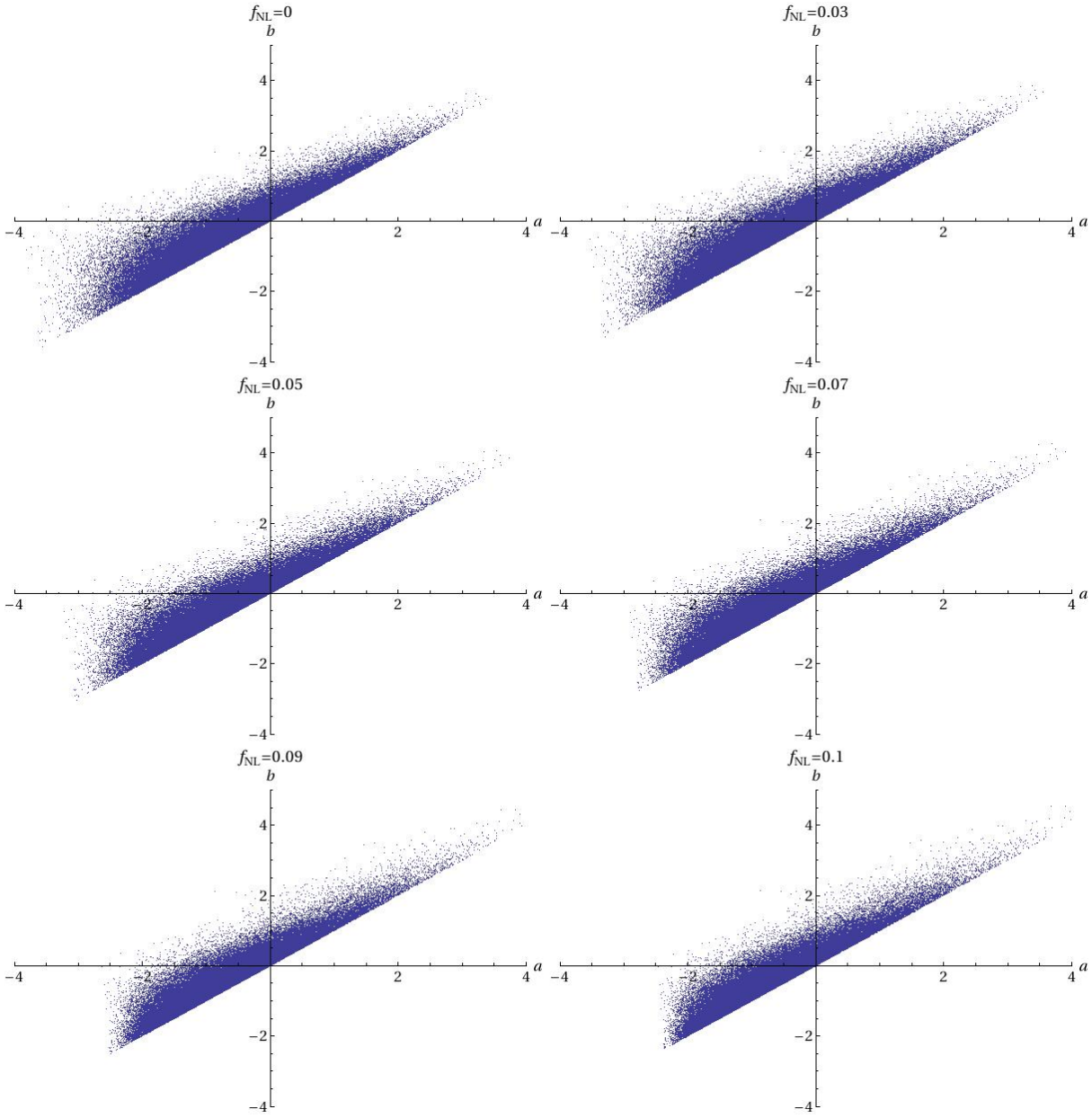

Figure 10.6: The top left figure shows the 0-dimensional persistence diagram of a realization of a Gaussian random field with a power law power spectrum with $n_s = -2$. The other figures show the 0−-dimensional persistence diagrams of the field with local non-Gaussianities imposed. It can be seen that the shape of the persistence diagram changes significantly as a function of the strength of non-Gaussianity f_{NL}.

Chapter 11

Conclusion

The characterization of the physics in the inflationary epoch of the universe are an active area of research in current cosmology and particle physics. The Cosmic Microwave Background (CMB) radiation seems to be a nearly Gaussian random field. The analysis of the deviations of this Gaussian random field form one of the main methods of inferring information about the physics in the early universe. Much research has recently been done on posing bounds on the amount of non-Gaussianities in the CMB, but those bounds are not yet strict enough to draw any rigid conclusions about inflationary physics.

In this thesis we have proposed a new method of analyzing non-Gaussianities in Gaussian random fields. We analyze the homological structure of Gaussian random fields using Betti numbers and persistence diagrams. We have shown that an analytical formula for the Betti numbers of such fields can be constructed and computed, given only the power spectrum of the field. Furthermore we have shown that an analytical formula to calculate the persistence diagrams of Gaussian random fields can be constructed. We have posed some limits on the character of this analytical formula, but we have not yet been able to complete the formalism to compute persistence diagrams analytically. More work needs to be done to find an analytical expression and thus to be able to analytically predict the persistence diagrams of Gaussian random fields..

In the second part of our research we have made realizations of Gaussian random fields and calculated their persistence diagrams. We have shown that persistence diagrams are a promising approach to learn more about the CMB and thus about inflationary physics. Nevertheless, different kinds of non-Gaussianities will need to be analyzed and work needs to be done on inferring information about the Gaussian random field and its non-Gaussianities from the persistence diagram of such a field. With the release of the Planck data in the coming year, our method could well provide some very strong bounds on f_{NL} and thus on the inflationary physics of our universe.

Many interesting research into the homology of Gaussian random fields remains, since this method of analyzing Gaussian random fields has only just started to make an impact on the research into non-Gaussianities. Different types of non-Gaussianities need to be analyzed, and the path to a fully analytical method of calculating persistence still

offers many challenges. Expanding the analysis we have done, and eventually applying the formalisms introduced to the CMB pose interesting research topics. Concluding, the homology of the universe remains an exiting area for future research.

Appendix A

Covariance matrices

A.1 Flat space

In order to calculate the covariance matrix M, of the random variable $y = (a, f_i(0), J_i(0), b, f_i(x), J_i(x))$, in flat space, we expand the field f in Fourier space and perform the derivatives. We then use the definition of the power spectrum to write M as a function of the power spectrum $P(k)$. For example:

$$
\begin{aligned}
f_1 &= \frac{\partial}{\partial r_1}\int \frac{d\mathbf{k}}{(2\pi)^2}\hat{f}(\mathbf{k})e^{-i\mathbf{k}\cdot\mathbf{r}} = -i\int \frac{d\mathbf{k}}{(2\pi)^2}\hat{f}(\mathbf{k})k_1 e^{-i\mathbf{k}\cdot\mathbf{r}} \\
\langle f_1 f_1^*\rangle &= \int \frac{d\mathbf{k}d\mathbf{p}}{(2\pi)^4}\langle\hat{f}(\mathbf{k})\hat{f}(\mathbf{p})\rangle k_1 p_1 e^{-i\mathbf{k}\cdot\mathbf{r}+i\mathbf{p}\cdot\mathbf{q}} \\
&= \int \frac{d\mathbf{k}}{(2\pi)^2}P(k)k_1^2 e^{-i\mathbf{k}(\mathbf{r}-\mathbf{q})}
\end{aligned}
$$

After taking $\mathbf{r} = (0,0)$and $\mathbf{q} = (0,x)$ and transforming to polar coordinates we obtain:

$$
\begin{aligned}
\langle f_1 f_1^*\rangle &= \int \frac{dk}{(2\pi)^2}P(k)k^3\int\ cos^2(\theta)e^{-i\sin(\theta)\cdot kx}d\theta \\
&= \int \frac{dk}{2\pi}P(k)k^3\frac{J_1(|kx|)}{|kx|}
\end{aligned}
$$

Using the same method as in the example above, we obtain the following relations for the other elements of M:

$$\begin{aligned}
\langle f f^* \rangle(\mathbf{x}) &= \xi(x) \\
\langle f_1 f_1^* \rangle(\mathbf{x}) &= -\langle f f_{11}^* \rangle(\mathbf{x}) = \int_0^\infty \frac{dk}{(2\pi)} k^3 P(k) \frac{J_1(kx)}{|kx|} \\
\langle f_2 f_2^* \rangle(\mathbf{x}) &= -\langle f f_{22}^* \rangle(\mathbf{x}) = \int_0^\infty \frac{dk}{(2\pi)} k^3 P(k) (\frac{J_1(kx)}{kx} - J_2(kx)) \\
\langle f_{11} f_{11}^* \rangle(\mathbf{x}) &= \int_0^\infty \frac{dk}{(2\pi)} k^5 P(k) \frac{3J_2(kx)}{(kx)^2} \\
\langle f_{11} f_{22}^* \rangle(\mathbf{x}) &= \langle f_{12} f_{12}^* \rangle(\mathbf{x}) = \int_0^\infty \frac{dk}{(2\pi)} k^5 P(k) \frac{kxJ_1(kx) - 3J_2(kx)}{(kx)^2} \\
\langle f_{22} f_{22}^* \rangle(\mathbf{x}) &= \langle f_{12} f_{12}^* \rangle(\mathbf{x}) = -\int_0^\infty \frac{dk}{(2\pi)} k^5 P(k) \frac{((kx)^2 - 3)J_2(kx)}{(kx)^2}.
\end{aligned}$$

All other correlation functions are 0.

By using Wick's formula [30] for 3 and 4-point correlation functions we obtain:

$$\begin{aligned}
\langle f J_1 \rangle(\mathbf{x}) =& \langle f f_{11} \rangle(\mathbf{x}) + \langle f f_{22} \rangle(\mathbf{x}) \\
\langle f(J_2 - 1) \rangle(\mathbf{x}) =& 0 \\
\langle J_1 J_1 \rangle(\mathbf{x}) =& \langle f_{11} f_{11} \rangle(\mathbf{x}) + \langle f_{22} f_{22} \rangle(\mathbf{x}) + 2\langle f_{11} f_{22} \rangle(\mathbf{x}) \\
\langle J_1(J_2 - 1) \rangle(\mathbf{x}) =& 0 \\
\langle (J_2 - 1)(J_2 - 1) \rangle(\mathbf{x}) =& \langle f_{11} f_{11} \rangle(0)^2 + 2\langle f_{11} f_{11} \rangle(x)^2 + \langle f_{11} f_{11} \rangle(0) \langle f_{22} f_{22} \rangle(0) \\
&+ 2\langle f_{11} f_{22} \rangle(x)^2 - 2\langle f_{11} f_{11} \rangle(0) \langle f_{11} f_{22} \rangle(0) \\
&- 4\langle f_{11} f_{11} \rangle(x) \langle f_{11} f_{22} \rangle(x) + \langle f_{22} f_{22} \rangle(0) \langle f_{11} f_{11} \rangle(0) \\
&+ 2\langle f_{22} f_{22} \rangle(x)^2 - 2\langle f_{22} f_{22} \rangle(0) \langle f_{11} f_{22} \rangle(0) \\
&- 4\langle f_{22} f_{11} \rangle(x) \langle f_{22} f_{22} \rangle(x) + 4\langle f_{11} f_{22} \rangle(0) \langle f_{11} f_{22} \rangle(0) \\
&+ 4\langle f_{11} f_{11} \rangle(x) \langle f_{22} f_{22} \rangle(x) + 4\langle f_{11} f_{22} \rangle(x)^2 - \langle f_{11} f_{11} \rangle(0) \\
&- \langle f_{22} f_{22} \rangle(0) + 2\langle f_{11} f_{22} \rangle(0) - \langle f_{11} f_{11} \rangle(0) \\
&- \langle f_{22} f_{22} \rangle(0) + 2\langle f_{11} f_{22} \rangle(0).
\end{aligned}$$

A.2 Spherical space

In order to apply the persistence theory to the Cosmic Microwave Background (CMB), one has to derive the co-variance matrix M for Gaussian random fields on the two dimensional sphere $\mathbb{S}^2$. Analogous to the Fourier expansion of the field for the flat case, we will expand the field in Spherical Harmonics for the field on the 2-sphere.

Given a Gaussian random field f, with spherical coordinates $\mathbf{n} = (\theta, \phi) \in \mathbb{S}^2$, the

field can be expanded in spherical harmonics using:

$$f(\mathbf{n}) = \sum_{l,m} a_{lm} Y_l^m(\hat{\mathbf{n}}),$$

where Y_l^m are spherical harmonics. Perform the summation,

$$\sum_m Y_l^m(\mathbf{n}_1) Y_l^m(\mathbf{n}_2) = \frac{2l+1}{4\pi} P_l(y),$$

where $n_i = (\theta_i, \phi_i)$, for $i = 1, 2$ are two points in $\mathbb{S}^2$, the function $P_l(y)$ is the Legendre polynomial and y is the distance between $\mathbf{n}_1$ and $\mathbf{n}_2$ given by $y = \cos(\theta_1)\cos(\theta_2) + \sin(\theta_1)\sin(\theta_2)\cos(\phi_1 - \phi_2)$. Differentiate the expression and substitute $(\theta_1, \phi_1) = (\pi/2, 0)$ and $(\theta_2, \phi_2) = (\pi/2, x)$ to obtain the required 2-point correlation function. For example:

$$\begin{aligned}
f_2 = \frac{\partial f}{\partial \phi} &= \sum_{l,m} a_{lm} \frac{\partial}{\partial \phi} Y_l^m(\hat{\mathbf{n}}) \\
\langle f_2 f_2^* \rangle(x) &= \sum_{l,m} \sum_{l',m'} \langle a_{lm} a_{a'm'}^* \rangle \frac{\partial}{\partial \phi_1} Y_l^m(\theta_1, \phi_1) \frac{\partial}{\partial \phi_2} Y_l^m(\theta_2, \phi_2) \\
&= \frac{\partial^2}{\partial \phi_1 \partial \phi_2} \sum_l \frac{2l+1}{4\pi} C_l P_l(y) \\
&= \sum_l \frac{2l+1}{4\pi} C_l \left[\frac{dP_l(y)}{dy} \cos(x) - \frac{d^2 P_l(y)}{dy^2} \sin^2(x) \right].
\end{aligned}$$

The exact analytic expression can be computed using Mathematica. The analytical expression is however too large to show here. The other 2-point functions can be computed in a similar fashion. In practice the terms $\langle f f_{11}^* \rangle$, $\langle f f_{12}^* \rangle$, $\langle f f_{22}^* \rangle$, $\langle f_{11} f_{11}^* \rangle$, $\langle f_{11} f_{12}^* \rangle$, $\langle f_{11} f_{22}^* \rangle$, $\langle f_{12} f_{12}^* \rangle$, $\langle f_{12} f_{22}^* \rangle$, $\langle f_{22} f_{22}^* \rangle$ and symmetric expressions are generally nonzero.

Using the property that the 3-point correlation function of a Gaussian random field is 0 and using Wick's or Isserlis' theorem for the 4-point correlation functions, one can calculate the co-variance matrix M from the above correlation functions, analogous to the calculation in flat space. Note that the expression will be slightly different due a few extra non zero correlations [18].

Bibliography

[1] R.J. Adler. *Random Fields and Geometry*. John Wiley & Sons, 1981.

[2] D. Babich, P. Creminelli, and M. Zaldarriaga. The shape of non-Gaussianities. *Journal of Cosmology and Astroparticle Physics*, 8:9, August 2004.

[3] Francisco Blanco-Silva. Triangulation of compact surfaces, 16:18:30 9 June 2012.

[4] Chao Chen and Michael Kerber. An output-sensitive algorithm for persistent homology. In *Symposium on Computational Geometry*, pages 207–216, 2011.

[5] X. Chen. Primordial Non-Gaussianities from Inflation Models. *Advances in Astronomy*, 2010, 2010.

[6] P. Creminelli, A. Nicolis, L. Senatore, M. Tegmark, and M. Zaldarriaga. Limits on non-Gaussianities from WMAP data. *Journal of Cosmology and Astroparticle Physics*, 5:4, May 2006.

[7] A. Curto, E. Martínez-González, R. B. Barreiro, and M. P. Hobson. Constraints on general primordial non-Gaussianity using wavelets for the Wilkinson Microwave Anisotropy Probe 7-year data. *Monthly notices of the royal astronomical society*, 417:488–494, October 2011.

[8] N. Dalal, O. Doré, D. Huterer, and A. Shirokov. Imprints of primordial non-Gaussianities on large-scale structure: Scale-dependent bias and abundance of virialized objects. *Physical Review D*, 77(12):123514, June 2008.

[9] A. Davidson, D. Karasik, and Y. Lederer. Higgs Driven Geodetic Evolution/Nucleation of de-Sitter Brane. *ArXiv High Energy Physics - Theory e-prints*, December 2001.

[10] Cecil Jose A Delfinado and Herbert Edelsbrunner. An incremental algorithm for betti numbers of simplicial complexes on the 3-sphere. *Computer Aided Geometric Design*, 12(7):771–784, 1995.

[11] A. G. Doroshkevich. Spatial structure of perturbations and origin of galactic rotation in fluctuation theory. *Astrophysics*, 6:320–330, October 1970.

[12] H. Edelsbrunner and J.L. Harer. *Computational Topology, An introduction.* AMS Press, 2009.

[13] H. Edelsbrunner and E. Muecke. Three-dimensional alpha shapes. *ACM Trans. Graphics*, 13:43–72.

[14] Herbert Edelsbrunner, John Harer, and Afra Zomorodian. Hierarchical morse complexes for piecewise linear 2-manifolds. In *Proceedings of the seventeenth annual symposium on Computational geometry*, SCG '01, pages 70–79, New York, NY, USA, 2001. ACM.

[15] Letscher D. Zomorodian A. Edelsbrunner, H. Topological persistance and simplification. *Discrete and Computational Geometry*, 28:511–533.

[16] Melott et al. Topology of large-scale structure. IV - Topology in two dimensions. *Astrophysical Journal*, 345:618–626, October 1989.

[17] Robert M. Gray. *Probability, Random Processes, and Ergodic Properties.* Springer-Verlag, 2010.

[18] Alan F. Heavens and Sujata Gupta. Full-sky correlations of peaks in the microwave background. *Monthly Notices of the Royal Astronomical Society*, 324:960, 2001.

[19] N. Kaiser A.S. Szalay J.M. Bardeen, J.R. Bond. The statistics of peaks of gaussian random fields. *Astrophysical journal part 1*, 304.

[20] S. Kachru, R. Kallosh, A. Linde, J. Maldacena, L. McAllister, and S. P. Trivedi. Towards inflation in string theory. *Journal of Cosmology and Astroparticle Physics*, 10:13, October 2003.

[21] E. Komatsu, J. Dunkley, M. R. Nolta, C. L. Bennett, B. Gold, G. Hinshaw, N. Jarosik, D. Larson, M. Limon, L. Page, D. N. Spergel, M. Halpern, R. S. Hill, A. Kogut, S. S. Meyer, G. S. Tucker, J. L. Weiland, E. Wollack, and E. L. Wright. Five-Year Wilkinson Microwave Anisotropy Probe Observations: Cosmological Interpretation. *Astrophysical Journal Supplement Series*, 180:330–376, February 2009.

[22] E. Komatsu et al. Seven-Year Wilkinson Microwave Anisotropy Probe (WMAP) Observations: Cosmological Interpretation. *Astrophys.J.Suppl.*, 192:18, 2011.

[23] E. Komatsu, A. Kogut, M. R. Nolta, C. L. Bennett, M. Halpern, G. Hinshaw, N. Jarosik, M. Limon, S. S. Meyer, L. Page, D. N. Spergel, G. S. Tucker, L. Verde, E. Wollack, and E. L. Wright. First-Year Wilkinson Microwave Anisotropy Probe (WMAP) Observations: Tests of Gaussianity. *Astrophysical Journal Supplement Series*, 148:119–134, September 2003.

[24] E. Komatsu, K. M. Smith, J. Dunkley, C. L. Bennett, B. Gold, G. Hinshaw, N. Jarosik, D. Larson, M. R. Nolta, L. Page, D. N. Spergel, M. Halpern, R. S. Hill, A. Kogut, M. Limon, S. S. Meyer, N. Odegard, G. S. Tucker, J. L. Weiland,

E. Wollack, and E. L. Wright. Seven-year Wilkinson Microwave Anisotropy Probe (WMAP) Observations: Cosmological Interpretation. *Astrophysical Journal Supplement Series*, 192:18, February 2011.

[25] E. Komatsu, K. M. Smith, J. Dunkley, C. L. Bennett, B. Gold, G. Hinshaw, N. Jarosik, D. Larson, M. R. Nolta, L. Page, D. N. Spergel, M. Halpern, R. S. Hill, A. Kogut, M. Limon, S. S. Meyer, N. Odegard, G. S. Tucker, J. L. Weiland, E. Wollack, and E. L. Wright. Seven-year Wilkinson Microwave Anisotropy Probe (WMAP) Observations: Cosmological Interpretation. *Astrophysical Journal Supplement Series*, 192:18, February 2011.

[26] Eiichiro Komatsu and David N. Spergel. Acoustic Signatures in the Primary Microwave Background Bispectrum. December 2000.

[27] M.S. Longuet-Higgins. Mathematical analysis of random noise. *Philosophical transactions of the royal society london A*, 249:321, 1957.

[28] Juan Maldacena. Non-gaussian features of primordial fluctuations in single field inflationary models. *Journal of High Energy Physics*, 2003(05):013, 2003.

[29] E. Muecke. *Shapes and Implementations in three-dimensional geometry.* PhD thesis.

[30] M.E. Peskin and D.V. Schroeder. *An introduction to Quantum Field Theory.* Westview Press, 1995.

[31] Dmitri Pogosyan, Christophe Pichon, and Christophe Gay. Non-gaussian extrema counts for cmb maps. *Physical Review D*, 84:083510, Oct 2011.

[32] S.O. Rice. Mathematical analysis of random noise. *Bell system technology journal*, 23.

[33] G I Rigopoulos and E P S Shellard. Non-linear inflationary perturbations. *Journal of Cosmology and Astroparticle Physics*, 2005(10):006, 2005.

[34] G. I. Rigopoulos, E. P. S. Shellard, and B. J. W. van Tent. Simple route to non-Gaussianity in inflation. *Physical review D*, 72(8):083507, October 2005.

[35] G.I. Rigopoulos, E.P.S. Shellard, and B.J.W. van Tent. Nonlinear perturbations in multiple-field inflation. *Physical review D.*

[36] Barbara Ryden. *An introduction to cosmology.* Pearson Addison-Wesley, 2003.

[37] A. Slosar, C. Hirata, U. Seljak, S. Ho, and N. Padmanabhan. Constraints on local primordial non-Gaussianity from large scale structure. *Journal of Cosmology and Astroparticle Physics*, 8:31, August 2008.

[38] D. N. Spergel, R. Bean, O. Doré, M. R. Nolta, C. L. Bennett, J. Dunkley, G. Hinshaw, N. Jarosik, E. Komatsu, L. Page, H. V. Peiris, L. Verde, M. Halpern, R. S.

Hill, A. Kogut, M. Limon, S. S. Meyer, N. Odegard, G. S. Tucker, J. L. Weiland, E. Wollack, and E. L. Wright. Three-Year Wilkinson Microwave Anisotropy Probe (WMAP) Observations: Implications for Cosmology. *Astrophysical Journal Supplement Series*, 170:377–408, June 2007.

[39] R. van de Weygaert and E. Bertschinger. Peak and gravity constraints in Gaussian primordial density fields: An application of the Hoffman-Ribak method. *Monthly Notices of the Royal Astronomical Society.*

[40] Rien van de Weygaert, Gert Vegter, Herbert Edelsbrunner, Bernard J. T. Jones, Pratyush Pranav, Changbom Park, Wojciech A. Hellwing, Bob Eldering, Nico Kruithof, E. G. P. (Patrick) Bos, Johan Hidding, Job Feldbrugge, Eline ten Have, Matti van Engelen, Manuel Caroli, and Monique Teillaud. Alpha, betti and the megaparsec universe: On the topology of the cosmic web. *Transactions on Computational Science*, 14:60–101, 2011.

[41] Christian Wagner and Licia Verde. N-body simulations with generic non-Gaussian initial conditions II: Halo bias. *Journal of Cosmology and Astroparticle Physics*, 1203:002.

[42] Christian Wagner, Licia Verde, and Lotfi Boubekeur. N-body simulations with generic non-Gaussian initial conditions I: Power Spectrum and halo mass function. *Journal of Cosmology and Astroparticle Physics*, 1010:022.

[43] Amit P. S. Yadav and Benjamin D. Wandelt. Primordial Non-Gaussianity in the Cosmic Microwave Background. July 2010.